A multidomain spectral method for supersonic reactive flows

Wai-Sun Don, David Gottlieb, Jae-Hun Jung [*],[1]

Division of Applied Mathematics, Brown University, 182 George Street, Providence, RI 02912, USA

Abstract

This paper has a dual purpose: it presents a multidomain Chebyshev method for the solution of the two-dimensional reactive compressible Navier–Stokes equations, and it reports the results of the application of this code to the numerical simulations of high Mach number reactive flows in recessed cavity. The computational method utilizes a newly derived interface boundary conditions as well as an adaptive filtering technique to stabilize the computations. The results of the simulations are relevant to recessed cavity flame-holders.
© 2003 Elsevier B.V. All rights reserved.

Keywords: Multidomain spectral method; Penalty interface conditions; Supersonic combustor; Recessed cavity flame-holder; Compressible Navier–Stokes equations

1. Introduction

The efficacy of spectral methods for the numerical solution of highly supersonic, reactive flows had been previously reported in the literature. Don and Gottlieb [7,8] simulated interactions of shock waves with hydrogen jets and obtained results showing the rich dynamics of the mixing process as well as the very complex shock structures. Don and Quillen [9] studied the interaction of a planar shock with a cylindrical volume of a light gas and showed that the spectral methods used gave good results for the flows with the shocks and complicated non-linear behaviors. In fact the results compared favorably to ENO schemes.

The methods reported above were based on Chebyshev techniques in one domain. In order to extend the utility of spectral methods to complex domains, multidomain techniques have to be considered. The main issue here is the stable imposition of the interface boundary conditions, and in this paper we consider mainly the penalty method, introduced for hyperbolic equations by Funaro and Gottlieb [10,11].

There is an extensive literature on the subject: Hesthaven [13–15] applied penalty BC for Chebyshev multidomain methods using the characteristic variables. Carpenter et. al. [4,21,22] used it in conjunction with compact finite difference schemes, going from a scalar model equation to the full N–S equations in

---

general coordinate systems. Carpenter et al. [5] demonstrated the conservation properties of the Legendre multidomain techniques.

In the current work we follow the same methodology but in the context of supersonic combustion. We formulate the stable interface conditions based on the penalty method in a conservative form for both Euler and Navier–Stokes equations in two-dimensional Cartesian coordinates. We derive stability conditions, independent on the local flow properties, for the penalty parameters for the Legendre spectral method. We also present here a new adaptive filtering technique that stabilize the spectral scheme when applied to supersonic reactive flows.

Implementing this method, we consider supersonic combustion problems in recessed cavities in order to establish the efficacy of recessed cavity flame-holders.

We consider two different cases: (1) *non-reactive flows with two chemical species* and (2) *reactive flows with four chemical species*.

Recessed cavities provide a high temperature, low speed recirculating region that can support the production of radicals created during chemical reactions. This stable and efficient flame-holding performance by the cavity is achieved by generating a recirculation region inside the cavity where a hot pool of radicals forms resulting in reducing the induction time and thus obtaining the auto-ignition [2,29]. Experiments have shown that such efficiency depends on the geometry of the cavity such as the degree of the slantness of the aft wall and the length to depth ratio of cavity L/D. Thus one can optimize the flame-holding performance by properly adjusting the geometrical parameters of the cavity flame-holder system for a given supersonic flight regime. There are two major issues of such cavity flame-holder system that need to be investigated: (1) *what is the optimal angle of the aft wall for a given L/D?* and (2) *how does the fuel injection interact with cavity flows?* An answer to these questions require both a comprehensive laboratory and numerical experiments.

There have been previous numerical studies on these questions, many of them rely on the turbulence models. Rizzetta [23] used a modification of the Baldwin–Lomax algebraic turbulence model. Davis and Bowersox [6] also used Baldwin–Lomax model. Zhang et.al. [30] used Wilcox κ–ω turbulence model. Baurle and Gruber [3] used the Menter model. Although the use of the turbulence models can make it possible to handle the compressible supersonic shear flows, the results are quite model-dependent as they require parametric assumptions. In this work, we solve the full compressible Navier–Stokes equations with chemical reactions without any turbulence model, using a multidomain spectral method.

Results of several numerical studies including the present study have shown that the stability of the recirculation inside cavity is enhanced for the lower angle of cavity compared to the rectangular cavity. The present study, however, gives more accurate and finer details of the fields than those done by lower order numerical experiments. We show that a stationary recirculation region is not formed inside the cavity contrary to what the lower order schemes predict. A quantitative analysis made in this study shows that the lower angled wall of the cavity reduces the pressure fluctuations significantly inside the cavity for the non-reactive flows. We obtained a similar result for the reactive flows with the ignition of the fuel supplied initially in the cavity.

The rest of this paper is organized as follows. In Section 2 the governing equations are given. In Section 3 we describe the numerical method used in this work. In this Section we present the adaptive filtering used to remove the high frequency mode that causes the instability due to the non-smoothness of the flow, and we derive stable penalty interface conditions. In Section 4 the system of the supersonic recessed cavity combustor is described. In Section 5 the main results of this work are given and discussed.

2. The governing equations

In this work, we consider the compressible Navier–Stokes equations in the presence of the chemical reactions. Since hydrogen is used as a fuel in our numerical experiments, four chemical species are considered, i.e., H_2, O_2, H_2O and N_2 with the chemical reaction between hydrogen and oxygen gases:

$$2H_2 + O_2 \rightleftharpoons 2H_2O \tag{1}$$

The two-dimensional compressible Navier–Stokes equations in conservative form can be written as

$$\frac{\partial q}{\partial t} + \frac{\partial F}{\partial x} + \frac{\partial G}{\partial y} = \frac{\partial F_v}{\partial x} + \frac{\partial G_v}{\partial y} + C. \tag{2}$$

The state vector, q, and the inviscid fluxes, F and G, are given by

$$q = \begin{pmatrix} \rho \\ \rho u \\ \rho v \\ E \\ \rho \mathbf{f} \end{pmatrix}, \quad F = \begin{pmatrix} \rho u \\ \rho u^2 + P \\ \rho u v \\ (E + P)u \\ \rho \mathbf{f_u} \end{pmatrix}, \quad G = \begin{pmatrix} \rho v \\ \rho u v \\ \rho v^2 + P \\ (E + P)v \\ \rho \mathbf{f_v} \end{pmatrix}. \tag{3}$$

Here ρ is the density, u and v are the mean mixture velocity components of flow, E is the total internal energy and P is the pressure. The mass fraction vector, is $\mathbf{f} = (f_1, f_2, f_3, f_4)^T$ and the column vectors $\mathbf{f}_u$ and $\mathbf{f}_v$ are composed of the specific momentum of ith species

$$\mathbf{f}_{u_i} = f_i(u + \tilde{u}_i), \quad \mathbf{f}_{v_i} = f_i(v + \tilde{v}_i). \tag{4}$$

The velocity field $(\tilde{u}_i, \tilde{v}_i)$ of the ith species is the drift velocity relative to the mean mixture velocity (u, v) and is determined by

$$(\tilde{u}_i, \tilde{v}_i) = \frac{\mu}{\rho S_c} \nabla f_i. \tag{5}$$

Here μ is the mixture dynamic viscosity to be determined in (11), and S_c is the Schmidt number which is taken to be 0.22. The viscous fluxes, F_v and G_v, are given by

$$F_v = \begin{pmatrix} 0 \\ \tau_{xx} \\ \tau_{yx} \\ u\tau_{xx} + v\tau_{yx} + \mu \frac{\bar{C}_p}{P_r} T_x - \rho \sum_{i=1}^{4} h_i \tilde{u}_i f_i \\ \mathbf{0} \end{pmatrix},$$

$$G_v = \begin{pmatrix} 0 \\ \tau_{xy} \\ \tau_{yy} \\ u\tau_{xy} + v\tau_{yy} + \mu \frac{\bar{C}_p}{P_r} T_y - \rho \sum_{i=1}^{4} h_i \tilde{v}_i f_i \\ \mathbf{0} \end{pmatrix}, \tag{6}$$

where $\mathbf{0} = (0, 0, 0, 0)^T$, T is the temperature, $\bar{C}_p$ is the mixture specific heat at constant pressure, P_r is the Prandtl number (which is taken to be 0.72) for the normal air and h_i is the specific enthalpy of the ith species and given by

$$h_i = h_i^0 + \int_0^T C_{p_i}(s) \, ds.$$

where h_i^0 is the reference enthalpy of the ith species and the specific heat of the ith species at constant pressure, C_{p_i} is represented as a fourth-order polynomial of T (see [20]). The elements of the viscous stress tensor are given by

$$\tau_{x_i x_j} = \mu \left(\frac{\partial u_i}{\partial x_j} + \frac{\partial u_j}{\partial x_i} \right) + \delta_{ij} \lambda \sum_{k=1}^{2} \frac{\partial u_k}{\partial x_k}, \tag{7}$$

where δ is the Kronecker delta symbol, and λ is the bulk viscosity which is taken to be $-\frac{2}{3}\mu$ under the Stokes hypothesis.

The equation of state is given by the assumption of the perfect gas law

$$P = \rho \bar{R} T = RT \sum_{i=1}^{4} \rho f_i / M_i, \tag{8}$$

where $\bar{R}$ is a mixture gas constant with the universal gas constant R and M_i is the molecular weights of ith species. The energy E is given by

$$E = \rho \int_0^T \bar{C}_p(s) \, \mathrm{d}s - P + \frac{1}{2}\rho(u^2 + v^2) + \sum_{i=1}^{4} \rho f_i h_i^0, \tag{9}$$

where the mixture specific heat at constant pressure is given by

$$\bar{C}_p = \sum_{i=1}^{4} C_{p_i} f_i / M_i. \tag{10}$$

2.1. The chemical models

We use the same models as in [7]. Each chemical species has different dynamical viscosity μ_i based on Sutherland's law and we obtain the mixture viscosity μ by Wilke's law [28], i.e.,

$$\frac{\mu_i}{\mu_{0_i}} = \left(\frac{T}{T_{0_i}} \right)^{3/2} \left(\frac{T_{0_i} + S_i}{T + S_i} \right)$$

$$\mu = \sum_{i=1}^{4} \frac{\mu_i f_i / M_i}{\sum_{j=1}^{4} f_j / M_j \phi_{ij}}, \tag{11}$$

$$\phi_{ij} = \frac{\left(1 + [(\mu_i/\mu_j)(f_j/f_i)]^{1/2}(M_i/M_j)^{1/4} \right)^2}{[8(1 + (M_i/M_j))]^{1/2}}.$$

Here μ_{0_i}, T_{0_i} and S_i are constants. A modified Arrhenius Law gives the equilibrium reaction rate k_e, the forward reaction rate k_f and the backward reaction rate k_b as

$$k_e = A_e T \exp(4.60517(E_e/T - 2.915)),$$
$$k_f = A_f \exp(-E_f/(RT)),$$
$$k_b = k_f/k_e,$$

where the activation energy $E_e = 12925$, $E_f = 7200$ and the frequency factor $A_e = 83.006156$, $A_f = 5.541 \times 10^{14}$.

The species are ordered as follows: (H_2, O_2, H_2O, N_2), and the law of mass action is used to find the net rate of change in concentration of ith species $\dot{C}_i$ by the single reaction (1), i.e.,

$$\dot{C}_1 = 2(k_f[H_2]^2[O_2] - k_b[H_2O]^2),$$
$$\dot{C}_2 = -(k_f[H_2]^2[O_2] - k_b[H_2O]^2),$$
$$\dot{C}_3 = 2(k_f[H_2]^2[O_2] - k_b[H_2O]^2),$$

where $[\cdot]$ denoted the net rate of change in concentration.

Finally, the chemical source term C in (2) is given by

$$C = (0, 0, 0, 0, \dot{C}_1 M_1, \dot{C}_2 M_2, \dot{C}_3 M_3, \dot{C}_4 M_4)^T, \tag{12}$$

where $\dot{C}_i$ is the net rate of change in concentration of ith species by the reaction.

In Appendix C, a table of all the necessary coefficients and constants used for the reactive Navier–Stokes equations with species (H_2, O_2, H_2O, N_2) are given.

3. The multidomain spectral method

In this section we describe the two crucial components of the Chebyshev multidomain code used in our work, i.e., the adaptive filtering and the penalty method for the stable interface conditions.

3.1. The adaptive filtering

It is well known that when pseudospectral methods are applied to nonlinear problems instabilities may occur. One of the ways to stabilize the spectral scheme is by adding a superviscosity term, or equivalently using low pass exponential filters.

Consider the system

$$\frac{\partial u}{\partial t} = \frac{\partial f(u)}{\partial x}. \tag{13}$$

The pseudospectral method involves an interpolation operator I_N that interpolates a function in the Gauss Lobato points (these relate to the zeroes of the derivative of Chebyshev or Legendre polynomials and include the boundaries or equally spaced points for the Fourier method). We seek a polynomial (or trigonometrical polynomial) u_N such that

$$\frac{\partial u_N}{\partial t} = \frac{\partial I_N f(u_N)}{\partial x}. \tag{14}$$

In the spectral superviscosity method we add a viscosity term such that

$$\frac{\partial u_N}{\partial t} = \frac{\partial I_N f(u_N)}{\partial x} + \epsilon_N SV u_N. \tag{15}$$

Here $\epsilon_N \sim (1/N^{2s-1})$ and the viscosity term SV is given as follows: it is

$$(-1)^{s-1} \frac{\partial^{2s}}{\partial x^{2s}}$$

for the Fourier method,

$$(-1)^{s-1} \left(\sqrt{1-x^2} \frac{\partial}{\partial x} \right)^{2s}$$

for the Chebyshev and

$$\left(\frac{\partial}{\partial x}(1-x^2)\frac{\partial}{\partial x}\right)^s$$

for the Legendre method. In order for this term to conform to the spectral accuracy, the order s must be proportional to N, the number of polynomials (or grid points) in the approximation. Thus if one refines the mesh the viscosity changes.

The theory developed by Tadmor [24], Maday and Tadmor [19], Maday et al. [18] and Ma [17] indicate that the numerical solution for the scalar case converges to the correct entropy condition. Carpenter et al. [5] demonstrated that even for systems, if the solution of (15) converges it converges to the correct entropy solution.

We note here that the parameter s can be a function of the spatial station x. This means that in different regions one uses different orders of the viscosity terms. Thus in the presence of local sharp gradients one should reduce the order of the filter (but it still should be an increasing function of N).

To understand the relationship between the superviscosity method and the filtering method used in this paper, let

$$u_N(x,t) = \sum_{k=0}^{N} a_k(t)\phi_k(x),$$

where ϕ_k are the basis function used that can be Fourier, Chebyshev or Legendre polynomial. Also, let $b_k(a_0, \ldots, a_N)$ be the coefficients in the expansion

$$I_N f(u_N) = \sum_{k=0}^{N} b_k(t)\phi_k(x).$$

Then (15) can be written as

$$\frac{\partial a_k}{\partial t} = b_k - c\epsilon_N k^{2s} a_k. \tag{16}$$

One gets

$$a_k(t+\Delta t) = \exp(-c\epsilon_N k^{2s}\Delta t)a_k(t) + \int_t^{t+\Delta t} \exp[-c\epsilon_N k^{2s}(t+\Delta t - \tau)]b_k(\tau)\,\mathrm{d}\tau.$$

Thus it is equivalent to the exponential filter, where both the solution and the derivatives are filtered.

We define the local adaptive filter by

$$u^\sigma = \sum_{k=0}^{N} \sigma\left(\frac{k}{N}\right)a_k(t)\phi(x). \tag{17}$$

Here

$$\sigma(\omega) = \exp(-\alpha\omega^{2\gamma s}), \tag{18}$$

where $\gamma = \gamma(x)$ changes in the domain. In practice one computes different u^σ and picks the one with heavy filtering in the presence of large gradients and the light filtered solution in smooth region. In Sections 4 and 5.1 we will show how we choose the different regions. As an alternative, consider again (15). Since ϵ_N is very small, the superviscosity term can be applied with lower order finite difference scheme. There were no difference in the results between these two ways of applying the schemes.

The *local adaptive filtering* keeps the scheme stable, without dissipating fine scale features away from this region. As discussed in Section 5 the results of this work indicate that the local adaptive filtering is applied only in a few number (in the range of 1–7) of grid points around the corner of the aft wall once in a while.

3.2. Stable interface conditions

In this paper we use mainly the penalty type interface conditions, i.e., the boundary conditions are imposed only in a weak form [10,11]. Successful penalty interface conditions were constructed based on the characteristics for the Navier–Stokes equations in [13–15] for spectral method and for high-order finite difference methods in [4,21,22], and a conservative form of penalty interface conditions was proposed [5] for the Legendre spectral method. Following the same idea as those works, we consider two interface conditions, i.e.,

1. *The averaging method*, in which the interface conditions are obtained by averaging the state vectors of the two adjacent domains.
2. *The penalty method in conservative form* in which the interface conditions are satisfied only in a weak form, leaving the approximations not necessarily continuous at the interfaces.

In the following sections we will give the penalty interface conditions for the Euler and Navier–Stokes equations and also show that the averaging method is a subset of the penalty method.

3.2.1. Conservative penalty interface conditions

Consider Eq. (2) with the inviscid part only, in the x-direction in the interval $-2 \leqslant x \leqslant 2$, i.e.,

$$\frac{\partial q}{\partial t} + \frac{\partial F}{\partial x} = 0. \tag{19}$$

For simplicity, assume that we have two domains in this interval with the interface at $x = 0$, $q_N^I(x, t)$ denotes the numerical solution in the left domain $x \leqslant 0$ and $q_M^{II}(x, t)$ in the right domain $x \geqslant 0$. Note that the numerical solution is composed of two polynomials of different orders. The Legendre spectral penalty method is given by

$$
\begin{aligned}
\frac{\partial q_N^I}{\partial t} + \frac{\partial I_N^I F(q_N^I)}{\partial x} &= B\big(q_N^I(-2, t)\big) + \tau_1 Q_N(x)\big[f^+\big(q_N^I(0, t)\big) - f^+\big(q_M^{II}(0, t)\big)\big] \\
&\quad + \tau_2 Q_N(x)\big[f^-\big(q_N^I(0, t)\big) - f^-\big(q_M^{II}(0, t)\big)\big], \\
\frac{\partial q_M^{II}}{\partial t} + \frac{\partial I_M^{II} F(q_M^{II})}{\partial x} &= B\big(q_M^{II}(2, t)\big) + \tau_3 Q_M(x)\big[f^+\big(q_M^{II}(0, t)\big) - f^+\big(q_N^I(0, t)\big)\big] \\
&\quad + \tau_4 Q_M(x)\big[f^-\big(q_M^{II}(0, t)\big) - f^-\big(q_N^I(0, t)\big)\big],
\end{aligned}
\tag{20}
$$

where B is a boundary operator at the end points, i.e., $x = \pm 2$ and I_N^I and I_M^{II} are the Legendre interpolation operators for the left and right domains, respectively. The positive and negative fluxes f^+ and f^- are defined by

$$f^{\pm} = \int S \Lambda^{\pm} S^{-1} \, \mathrm{d}q, \tag{21}$$

with

$$A \equiv \frac{\partial E}{\partial q} = S \Lambda S^{-1}. \tag{22}$$

The Jacobian matrix A is assumed to be symmetric. Λ^+ and Λ^- are the diagonal matrices composed of positive and negative eigenvalues of A, respectively. $Q_N(x)$ and $Q_M(x)$ are polynomials of orders N and M, respectively, such that they are zero at all the collocation points except the interface points $x = 0$ (for example $Q_M(x) = (1 - x/2) T_M'(x/2)/M^2$, $0 \leqslant x \leqslant 2$ where $T_M(x)$ is the Chebyshev polynomial of degree M). The penalty parameters τ_1, τ_2, τ_3 and τ_4 are all constants. Since we are interested only in the interface

conditions, we ignore the boundary operator B at $x = \pm 2$. Define the discrete scalar product $(p, q)_N = \sum_{i=0}^{N} p^{\mathrm{T}}(\xi_i) q(\xi_i) \omega_i$. ω_i is the weight in the Gauss–Lobatto–Legendre quadrature formula. With the discrete product, the energy $E(t)$ is defined by $E(t) = (q_N^I(x,t), q_N^I(x,t))_N + (q_M^{II}(x,t), q_M^{II}(x,t))_M$.

Theorem 1 (Conservativity). *The scheme given in Eq. (20) is conservative if the penalty parameters satisfy the following conditions*:

$$\tau_1 \omega_N^I - \tau_1 \omega_M^{II} = 1, \quad \tau_2 \omega_N^I - \tau_4 \omega_M^{II} = 1. \tag{23}$$

Proof. Based on the assumption above on the boundary operator B it suffices to consider only the penalty terms to prove the theorem. Define the Legendre weight vectors $\vec{\omega}_N^I$ and $\vec{\omega}_M^{II}$ for Ω^I and Ω^{II} such that

$$\vec{\omega}_N^I = \left(\omega_0^I, \dots, \omega_N^I\right), \quad \vec{\omega}_M^{II} = \left(\omega_0^{II}, \dots, \omega_M^{II}\right).$$

Multiply the equations for q_N^I and q_M^{II} in (20) by $\vec{\omega}_N^I$ and $\vec{\omega}_M^{II}$. Then using the quadrature rule we have

$$\int_{-2}^{0} \frac{\partial q_N^I}{\partial t} \mathrm{d}x + \int_{0}^{2} \frac{\partial q_M^{II}}{\partial t} \mathrm{d}x = -\int_{-2}^{0} \frac{\partial f_N^I}{\partial x} \mathrm{d}x - \int_{0}^{2} \frac{\partial f_M^{II}}{\partial x} \mathrm{d}x + \tau_1 \left[f^+(q_N^I(0,t)) \omega_N^I - f^+(q_M^{II}(0,t)) \omega_0^{II} \right]$$
$$+ \tau_2 \left[f^-(q_N^I(0,t)) \omega_N^I - f^-(q_M^{II}(0,t)) \omega_0^{II} \right] + \tau_3 \left[f^+(q_M^{II}(0,t)) \omega_0^{II} \right.$$
$$\left. - f^+(q_N^I(0,t)) \omega_N^I \right] + \tau_4 \left[f^-(q_M^{II}(0,t)) \omega_0^{II} - f^-(q_N^I(0,t)) \omega_N^I \right]. \tag{24}$$

By the fact that $\int (\partial f_N / \partial x) \mathrm{d}x = f^+ + f^-$ and $\omega_0^{II} = \omega_M^{II}$ the RHS of the above equation becomes

$$\mathrm{RHS} = \left(f^+(q_N^I(0,t)) - f^+(q_M^{II}(0,t)) \right) \left[\tau_1 \omega_N^I - \tau_3 \omega_M^{II} - 1 \right] + \left(f^-(q_N^I(0,t)) - f^-(q_M^{II}(0,t)) \right) \left[\tau_2 \omega_N^I - \tau_4 \omega_M^{II} - 1 \right].$$

Thus if $\tau_1 \omega_N^I - \tau_1 \omega_M^{II} = 1$ and $\tau_2 \omega_N^I - \tau_4 \omega_M^{II} = 1$ then the LHS vanishes and this prove the theorem. $\square$

Theorem 2. *The energy is bounded by the initial energy of the system if the following conditions are satisfied* [5]:

$$2\omega_N^I \tau_1 \leqslant 1, \quad 2\omega_N^I \tau_2 \geqslant 1, \quad 2\omega_M^{II} \tau_3 \leqslant -1, \quad 2\omega_M^{II} \tau_4 \geqslant -1,$$
$$\omega_N^I \tau_1 - \omega_M^{II} \tau_3 = 1, \quad \omega_N^I \tau_2 - \omega_M^{II} \tau_4 = 1. \tag{25}$$

3.2.2. The penalty method for the Euler equations

The penalty method in the case of the two-dimensional Euler equation is given by

$$\frac{\partial q_N}{\partial t} + \frac{\partial I_N F(q_N)}{\partial x} + \frac{\partial I_N G(q_N)}{\partial y} = \tau_{1,3} Q(x,y) [f^+(q_N) - f^+(q_{M-})] + \tau_{2,4} Q(x,y) [f^-(q_N) - f^-(q_{M-})], \tag{26}$$

where q_{M-} is the state vector of the adjacent domain at the interface of degree M, $\tau_{1,3}(\tau_{2,4})$ denotes $\tau_1(\tau_2)$ and $\tau_3(\tau_4)$, respectively. τ_1 and τ_2 (τ_3 and τ_4) are the penalty parameters for the right(left) in x-direction and top(bottom) in y-direction, respectively. $Q(x,y)$ is a polynomial which vanishes at all of interior points of the domain and is equal to 1 at the four interfaces. Note that the boundary operator B does not appear in the scheme. Let A be the linearized Jacobian matrix (around a state vector q_0) of two inviscid fluxes

$$A = \left(\frac{\partial F}{\partial q}, \frac{\partial G}{\partial q} \right) \cdot \vec{n} \bigg|_{q_0}, \tag{27}$$

where $\vec{n} = (n_x, n_y)$ is the unit outward normal vector. Since the matrix A is symmetric, there exists S such that

$$A = S \Lambda S^{-1}, \tag{28}$$

where Λ is a diagonal matrix composed of eigenvalues of A. Then $A = A^+ + A^-$ and $A^\pm = S\Lambda^\pm S^{-1}$. $A^\pm$ is defined as in previous section. Splitting A yields

$$f^\pm = A^\pm q_0, \tag{29}$$

where $f^\pm$ is obtained from the linearized state.

Remark 1. Since $\vec{n} = (n_x, n_y)$ is taken to be outward normal vector, the stability condition (25) is now modified and given as

$$2\omega_N^I \tau_1 \leqslant 1, \quad 2\omega_N^I \tau_2 \geqslant 1, \quad 2\omega_M^{II} \tau_3 \leqslant 1, \quad 2\omega_M^{II} \tau_4 \geqslant 1,$$
$$\omega_N^I \tau_1 + \omega_M^{II} \tau_4 = 1, \quad \omega_N^I \tau_2 + \omega_M^{II} \tau_3 = 1. \tag{30}$$

The Jacobian matrix A and its eigenvalue matrix Λ are given in Appendix A.

For illustration, we consider the propagation of a Gaussian density peak at the center of rectangular physical domains. The physical domain is partitioned with 16 sub-domains. The interface conditions between the domains are imposed according to the penalty Euler equations as discussed above. Characteristic boundary conditions are imposed at the outer physical boundaries. The results presented in Fig. 1 indicate that the penalty formulation works well. From the numerical experiments of this problem, we observe that reflections can be created at the interface across the adjacent domains depending on the choice of the penalty parameters. Thus proper choice of the penalty parameters should take into account reflections from the interfaces. To demonstrate the above formulation for the Euler equations, we will return to this issue in a future paper [16].

3.2.3. The penalty method for the Navier–Stokes equations

When dealing with the Navier–Stokes equation, we keep the penalty form for the Euler fluxes and add a penalty term for the viscous fluxes. The stability of this procedure stems from the fact that the Jacobian matrices for the full reactive Navier–Stokes equation can be symmetrized by the same similarity transformation (see Appendix B). Thus we get the system

$$\begin{aligned} \frac{\partial q_N}{\partial t} + \frac{\partial I_N F}{\partial x} + \frac{\partial I_N G}{\partial y} = &\frac{\partial I_N F_v}{\partial x} + \frac{\partial I_N G_v}{\partial y} + \tau_{1,3} Q(x,y)[f^+(q_N) - f^+(q_{M-})] \\ &+ \tau_{2,4} Q(x,y)[f^-(q_N) - f^-(q_{M-})] + \tau_{6,8} Q(x,y)[\mathbf{A}_v \cdot \mathbf{q}_N - \mathbf{A}_v \cdot \mathbf{q}_{M-}] \\ &+ \tau_{5,7} Q(x,y)[\mathbf{A}_v \cdot \partial \mathbf{q}_N - \mathbf{A}_v \cdot \partial \mathbf{q}_{M-}]. \end{aligned} \tag{31}$$

Here $f^\pm$ are same as defined in the previous section and the Jacobian matrix vector $\mathbf{A}_v$ is given by

$$\mathbf{A}_v = \left(\frac{\partial F_v}{\partial q_x} n_x, \frac{\partial G_v}{\partial q_y} n_y \right) \Bigg|_{q_0} \tag{32}$$

and

$$\mathbf{q} = (q, q), \quad \partial \mathbf{q} = (q_x, q_y), \tag{33}$$

where again $\mathbf{q}_-$ and $\partial \mathbf{q}_-$ denote the adjacent domains state vectors and their derivatives. Note that the penalty terms $\mathbf{A}_v \cdot \partial \mathbf{q}$ does not appear in [4,21,22]. The penalty parameters $\tau_{5,7}$ and $\tau_{6,8}$ are defined in the same way as in the previous section. To seek stable penalty parameters we split the inviscid and viscous fluxes and keep the stability conditions of $\tau_{1,2,3,4}$ for the inviscid flux as in Theorem 2. The stability conditions of $\tau_{5,7}$ and $\tau_{6,8}$ are given in the following theorem:
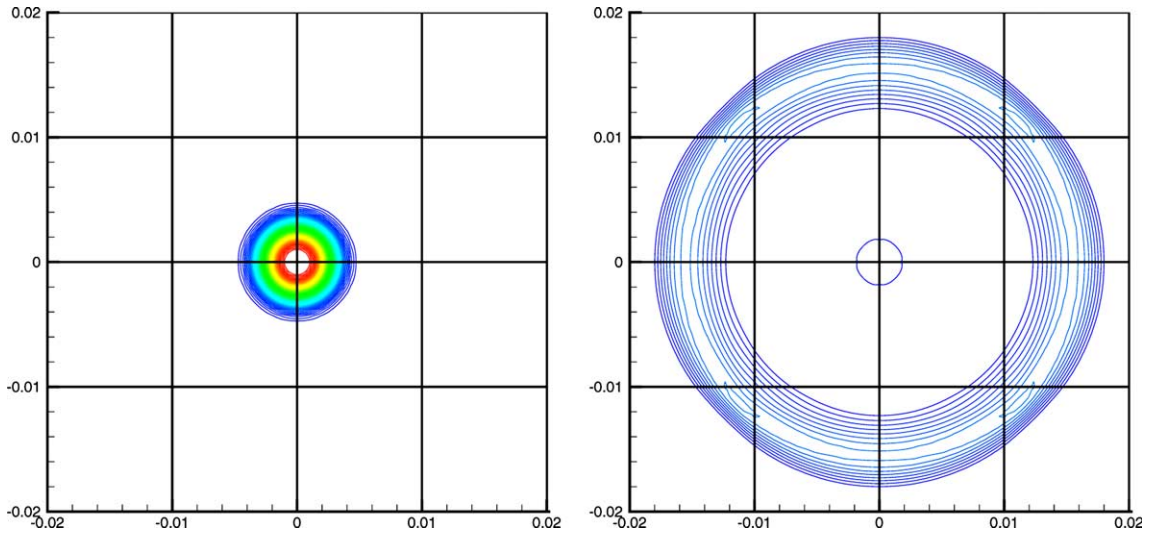
Fig. 1. The propagation of a density peak with the penalty Euler equations with 16 sub-domains: the initial condition (left) and the solution (right) at $t = 0.03604$ ms are given.

Theorem 3. *The penalty method for the Navier–Stokes equations* (31) *is stable if the penalty parameters τ_j, $j = 1, \ldots, 4$ are as in Theorem 2 and the rest satisfy*

$$\omega_N \tau_6 \leqslant 0,$$
$$\omega_N \tau_6 - \omega_M \tau_8 = 0,$$
$$1 + \omega_N \tau_5 - \omega_M \tau_7 = 0,$$

$$\left(\frac{1}{\omega_M} + \frac{1}{\omega_N} \right) \omega_M^2 \tau_7^2 - 2\tau_7 + 4\omega_N \tau_6 + \frac{1}{\omega_M} \leqslant 0. \tag{34}$$

Proof. As in the proof of Theorem 2, we assume that we have two domains and by multiplying the equations by the state vectors, we get

$$\frac{1}{2} \frac{\mathrm{d}}{\mathrm{d}t} E(t) \leqslant [Inviscid] + [Viscous], \tag{35}$$

where [*Inviscid*] and [*Viscous*] denote the terms from inviscid and viscous parts of the equation, respectively. The conditions for $\tau_{1,2}$ and $\tau_{3,4}$ given in Theorem 2 assure that the first term [*Inviscid*] is negative. The [*Viscous*] part at the interface is given by

$$[Viscous] = q^{\mathrm{T}} A_v q' - \sum_{i=0}^{N} q_i'^{\mathrm{T}} A_v q_i' \omega_i - q_-^{\mathrm{T}} A_v q_-' - \sum_{j=0}^{M} q_{i-}'^{\mathrm{T}} A_v q_{i-}' \omega_j + \tau_5 \omega_N [q^{\mathrm{T}} A_v q' - q^{\mathrm{T}} A_v q_-']$$
$$+ \tau_7 \omega_M [q_-^{\mathrm{T}} A_v q_-' - q_-^{\mathrm{T}} A_v q'] + \tau_6 \omega_N [q^{\mathrm{T}} A_v q - q^{\mathrm{T}} A_v q_-] + \tau_8 \omega_M [q_-^{\mathrm{T}} A_v q_- - q_-^{\mathrm{T}} A_v q], \tag{36}$$

where q' denotes the derivative of q either in x- or y-direction, ω is the Legendre weight, and A_v is

$$A_v = \left(\frac{\partial F_v}{\partial q_x}, \frac{\partial G_v}{\partial q_y} \right) \cdot \vec{n} \Big|_{q_0}. \tag{37}$$

Since all the eigenvalues of A_v are non-negative, every term inside the summations in the above equation is not negative, and we would like to keep the boundary terms. Thus we get the energy estimate such as

$$\frac{1}{2}\frac{\mathrm{d}}{\mathrm{d}t}E(t) \leqslant [q^{\mathrm{T}}A_v q' - \omega_N q'^{\mathrm{T}}A_v q' - q_-^{\mathrm{T}}A_v q'_- - \omega_M q'^{\mathrm{T}}_-A_v q'_-] + \tau_5 \omega_N [q^{\mathrm{T}}A_v q' - q^{\mathrm{T}}A_v q'_-]$$
$$+ \tau_7 \omega_M [q_-^{\mathrm{T}}A_v q'_- - q_-^{\mathrm{T}}A_v q'] + \tau_6 \omega_N [q^{\mathrm{T}}A_v q - q^{\mathrm{T}}A_v q_-] + \tau_8 \omega_M [q_-^{\mathrm{T}}A_v q_- - q_-^{\mathrm{T}}A_v q]. \tag{38}$$

The RHS of (38) can be rewritten as

$$\mathrm{RHS} = u^{\mathrm{T}}Bu, \tag{39}$$

where $u = (q, q_-, q', q'_-)$ and B is given by

$$B = \begin{pmatrix} 2\sigma_6 A_v & -\sigma_6 A_v - \sigma_8 A_v^{\mathrm{T}} & (1+\sigma_5)A_v & -\sigma_5 A_v \\ -\sigma_6 A_v^{\mathrm{T}} - \sigma_8 A_v & 2\sigma_8 A_v & -\sigma_7 A_v & (-1+\sigma_7)A_v \\ (1+\sigma_5)A_v^{\mathrm{T}} & -\sigma_7 A_v^{\mathrm{T}} & -2\omega_N A_v & \mathbf{0} \\ -\sigma_5 A_v^{\mathrm{T}} & (-1+\sigma_7)A_v^{\mathrm{T}} & \mathbf{0} & -2\omega_M A_v \end{pmatrix} \tag{40}$$

with $\mathbf{0} = \mathrm{diag}(0,0,0,0)$, $\sigma_5 = \omega_N \tau_5$, $\sigma_6 = \omega_N \tau_6$, $\sigma_7 = \omega_M \tau_7$ and $\sigma_8 = \omega_M \tau_8$. It is sufficient for the proof if B can be shown to be negative semi-definite. This first leads to

$$\omega_N \tau_6 \leqslant 0, \quad \omega_N \tau_6 = \omega_M \tau_8, \quad 1 + \omega_N \tau_5 - \omega_M \tau_7 = 0. \tag{41}$$

Note that we use here the fact that A_v is symmetrizable (see Appendix B). Taking into account (41), B becomes

$$B = \begin{pmatrix} 2\sigma_6 & -\sigma_7 & -1+\sigma_7 \\ -\sigma_7 & -2\omega_N & 0 \\ -1+\sigma_7 & 0 & -2\omega_M \end{pmatrix}. \tag{42}$$

To ensure negative semi-definiteness, $\det(B) \leqslant 0$ and therefore

$$\left(\frac{1}{\omega_M} + \frac{1}{\omega_N}\right)\sigma_7^2 - 2\frac{1}{\omega_M}\sigma_7 + 4\sigma_6 + \frac{1}{\omega_M} \leqslant 0. \tag{43}$$

Thus

$$\sigma_7^- \leqslant \sigma_7 \leqslant \sigma_7^+, \tag{44}$$

where

$$\sigma_7^{\pm} = \frac{\omega_N}{\omega_M + \omega_N} \pm \sqrt{\frac{(\omega_N \omega_M)(1 - 4\sigma_6(\omega_M + \omega_N))}{(\omega_N + \omega_M)^2}}.$$

Here we note that the condition that $\sigma_6 \leqslant \{-1/[4(\omega_N + \omega_M)]\}$ must be also satisfied in order for σ_7 to have real root. This yields the conditions in the theorem. $\square$

Note that these conditions are given independently of the local flow properties. And moreover, the penalty parameters of each domain are constrained by its adjacent domain.

Remark 2. For $\vec{n}$ to be outward normal vector the condition (34) is now given by

$$\omega_N \tau_6 \leqslant 0, \quad \omega_N \tau_6 + \omega_M \tau_8 = 0, \quad 1 + \omega_N \tau_5 + \omega_M \tau_7 = 0,$$

$$\left(\frac{1}{\omega_M}+\frac{1}{\omega_N}\right)\omega_M^2\tau_7^2+2\tau_7+4\omega_N\tau_6+\frac{1}{\omega_M}\leqslant 0, \tag{45}$$

with conditions (30).

Remark 3. If the interval of each domain is different then scheme (20) is not conservative. Let Δ^I and Δ^{II} be the domain intervals of Ω^I and Ω^{II}, respectively. The RHS in Theorem 1 becomes

$$\mathrm{RHS}=f^+\left(q_N^I(0,t)\right)\left[\tau_1\omega_N^I-\tau_3\omega_M^{II}-\frac{\Delta^I}{2}\right]+f^+\left(q_M^{II}(0,t)\right)\left[\tau_3\omega_M^{II}-\tau_1\omega_N^I-\frac{\Delta^{II}}{2}\right]$$
$$+f^-\left(q_N^I(0,t)\right)\left[\tau_1\omega_N^2-\tau_4\omega_M^{II}-\frac{\Delta^I}{2}\right]+f^-\left(q_M^{II}(0,t)\right)\left[\tau_4\omega_M^{II}-\tau_2\omega_N^I-\frac{\Delta^{II}}{2}\right].$$

For any $f^\pm(0,t)$ (note that $f^\pm(q_N^I(0,t))\neq f^\pm(q_M^{II}(0,t))$ in general) the RHS vanishes only when $\Delta^I=\Delta^{II}$. Thus in order to refine a particular sub-domain but still maintain the conservativity, one can use p-refinement rather than h-refinement such that $\Delta^I=\Delta^{II}$ but $N\neq M$.

3.2.4. The averaging method

We show in this section that the averaging method can also be written as a penalty method with a particular choice of the parameters.

3.2.5. Euler equations

We start first with the Euler equations. Consider the following penalty method:

$$\frac{\partial q}{\partial t}+\frac{\partial F}{\partial x}+\frac{\partial G}{\partial y}=\tau_{1,3}Q(x,y)[f'^+(q)-f'^+(q_-)]+\tau_{2,4}Q(x,y)[f'^-(q)-f'^-(q_-)], \tag{46}$$

where

$$f'^\pm=\left(A^\pm q_x,A^\pm q_y\right)\cdot\vec{n}\big|_{q_0}, \tag{47}$$

Note that the penalty terms use the derivative of the fluxes.

Theorem 4. If $\tau_1=\tau_3=\frac{1}{2}$, $\tau_2=\tau_4=\frac{1}{2}$, then the above penalty method (46) is equivalent to the averaging method and is stable.

Proof. We prove the theorem at the interface $x=0$ with the rectangular domain and assume that $N=M$. If $\tau_1=\tau_3=\frac{1}{2}$ and $\tau_2=\tau_4=\frac{1}{2}$, then the method becomes

$$\frac{\partial q^I}{\partial t}\bigg|_{x=0}=\frac{\partial q^{II}}{\partial t}\bigg|_{x=0}=-\frac{1}{2}\left(\frac{\partial F^I}{\partial x}+\frac{\partial F^{II}}{\partial x}\right)-\frac{\partial G}{\partial y} \tag{48}$$

and this is obviously equivalent to the averaging method. Here note that $(\partial G^I/\partial y)=(\partial G^{II}/\partial y)=(\partial G^{II}/\partial y)$. Following the same procedure in Theorem 3, the energy equation becomes

$$\frac{1}{2\omega_N}\frac{\mathrm{d}}{\mathrm{d}t}E(t)=-\frac{1}{2\omega_N}(q^I Aq^I-q^{II}Aq^{II})|_0+(\tau_1 q^I-\tau_3 q^{II})A^+(q_x^I-q_x^{II})|_0+(\tau_2 q^I-\tau_4 q^{II})A^-(q_x^I-q_x^{II})|_0. \tag{49}$$

Since $\tau_1=\tau_3=\frac{1}{2}$, $\tau_2=\tau_4=\frac{1}{2}$, and $q^I(0,y,t)=q^{II}(0,y,t)$, the RHS of the above equation vanishes and the energy is bounded by the initial energy. □

Remark 4 (*Conservativity*). If the condition is satisfied in the above theorem, scheme (46) is conservative.

Proof. By multiplying Eq. (46) by the weight vectors ω_N^I and ω_M^{II} and using the condition we have

$$\int_{-2}^0 \frac{\partial q_N^I}{\partial t}\,\mathrm{d}x + \int_0^2 \frac{\partial q_N^{II}}{\partial t}\,\mathrm{d}x = -\int_{-2}^0 \frac{\partial f_N^I}{\partial x}\,\mathrm{d}x - \int_0^2 \frac{\partial f_N^{II}}{\partial x}\,\mathrm{d}x + \frac{1}{2}\left[f_x(q_N^I(0,t))\omega_N^I - f_x(q_N^{II}(0,t))\omega_0^{II}\right]$$

$$+ \frac{1}{2}\left[f_x(q_N^{II}(0,t))\omega_0^{II} - f_x(q_N^I(0,t))\omega_N^I\right].$$

Thus without the consideration of the outer boundaries, the RHS of the above equation becomes with $N = M$ (see Remark 5)

$$\mathrm{RHS} = -f_N^I\big(q_N^I(0,t)\big) + f_N^{II}\big(q_N^{II}(0,t)\big).$$

The above equation says that $q_N^I(0,t) = q_N^{II}(0,t)$ and thus $f_N^I(q_N^I(0,t)) = f_N^{II}(q_N^{II}(0,t))$. Thus the RHS vanishes. □

The Navier–Stokes equations. The averaging method for the N–S equations can be presented as

$$\frac{\partial q}{\partial t} + \frac{\partial F}{\partial x} + \frac{\partial G}{\partial y} = \frac{\partial F_v}{\partial x} + \frac{\partial G_v}{\partial y} + \tau_{1,3}Q(x,y)[f'^+(q) - f'^+(q_-)] + \tau_{2,4}Q(x,y)[f'^-(q) - f'^-(q_-)]$$

$$+ \tau_{5,7}Q(x,y)[\mathbf{A}_v \cdot \partial^2\mathbf{q} - \mathbf{A}_v \cdot \partial^2\mathbf{q}_-] + \tau_{6,8}Q(x,y)[\mathbf{A}_v \cdot \partial\mathbf{q} - \mathbf{A}_v \cdot \partial\mathbf{q}_-], \tag{50}$$

where $\partial^2\mathbf{q}$ is the second derivative of q in either x- or y-direction.

Theorem 5. *If* $\tau_1 = \tau_3 = \frac{1}{2}$, $\tau_2 = \tau_4 = \frac{1}{2}$, $\tau_5 = \tau_7 = \frac{1}{2}$, *and* $\tau_6 = -\tau_8 = -1/2\omega_N$, *then the approximation is continuous at the interface and the scheme* (50) *is stable.*

Proof. If $\tau_1 = \tau_3 = \frac{1}{2}$, $\tau_2 = \tau_4 = \frac{1}{2}$, $\tau_5 = \tau_7 = \frac{1}{2}$, and $\tau_6 = -\tau_8 = -1/\omega_N$, then (50) becomes

$$\frac{\partial q^I}{\partial t}\bigg|_{x=0} = \frac{\partial q^{II}}{\partial t}\bigg|_{x=0} = -\frac{1}{2}\left(\frac{\partial F^I}{\partial x} + \frac{\partial F^{II}}{\partial x}\right) - \frac{\partial G}{\partial y} + \frac{1}{2}\left(\frac{\partial F_v^I}{\partial x} + \frac{\partial F_v^{II}}{\partial x}\right) + \frac{\partial G_v}{\partial y} + \frac{1}{\omega_N}\mathbf{A}_v \cdot (\partial\mathbf{q}^{II} - \partial\mathbf{q}^I), \tag{51}$$

and this ensures the continuity of the approximation at the interface. If the approximation is smooth enough such that the derivative of q is continuous at the interface then this becomes the averaging method.

Thus we get for the energy

$$\frac{1}{2\omega_N}\frac{\mathrm{d}}{\mathrm{d}t}E(t) = -\frac{1}{2\omega_N}\left(q^I A q^I - q^{II} A q^{II} - 2q^I A_v q_x^I + 2q^{II} A_v q_x^{II}\right)\big|_{x=0} - \int_{-2}^0 q_x^I A_v q_x^I\,\mathrm{d}x - \int_0^2 q_x^{II} A_v q_x^{II}\,\mathrm{d}x$$

$$+ \left[(\tau_1 q^I - \tau_3 q^{II})A^+ + (\tau_2 q^I - \tau_4 q^{II})A^-\right](q_x^I - q_x^{II})\big|_{x=0} + \left[(\tau_5 q^I - \tau_7 q^{II})A_v(q_{xx}^I - q_{xx}^{II})\right.$$

$$+ \left.(\tau_6 q^I - \tau_8 q^{II})A_v(q_x^I - q_x^{II})\right]\big|_{x=0}. \tag{52}$$

Since $q^I(0,y,t) = q^{II}(0,y,t)$, we have

$$\frac{1}{2\omega_N}\frac{\mathrm{d}}{\mathrm{d}t}E(t) \leqslant q^I\left(\left[(\tau_1 - \tau_3)A^+ + (\tau_2 - \tau_4)A^-\right](q_x^I - q_x^{II}) + (\tau_5 - \tau_7)A_v\big(q_{xx}^I - q_{xx}^{II}\big)\right.$$

$$\left. \times \left(\tau_6 - \tau_8 + \frac{1}{\omega_N}\right)A_v\big(q_x^I - q_x^{II}\big)\right)\bigg|_{x=0}. \tag{53}$$

Thus if $\tau_1 = \tau_3 = \frac{1}{2}$, $\tau_2 = \tau_4 = \frac{1}{2}$, $\tau_5 = \tau_7 = \frac{1}{2}$, and $\tau_6 = -\tau_8 = -1/2\omega_N$, the RHS vanishes. □

Remark 5. In the above averaging theorems if $N \neq M$ then the RHS of the equation of the energy estimates does not vanish. For example if $N \neq M$ the RHS of Eq. (49) becomes

$$\text{RHS} = \frac{1}{2}\left(\omega_N q_N^I - \omega_M q_N^{II}\right)A^+\left(q_x^I - q_x^{II}\right)\big|_{x=0} + \frac{1}{2}\left(\omega_N q_N^I - \omega_M q_N^{II}\right)A^-\left(q_x^I - q_x^{II}\right)\big|_{x=0}$$

$$= \frac{1}{2}q_N^I(\omega_N - \omega_M)A\left(q_x^I - q_x^{II}\right)\big|_{x=0},$$

where we use that $q_N^I(0,t) = q_M^{II}(0,t)$ and $\tau_1 = \tau_2 = \tau_3 = \tau_4 = \frac{1}{2}$. Thus if $N \neq M$ it does not necessarily vanish. Thus with Eq. (3) the averaging method requires that $\Delta^I = \Delta^{II}$ and $N = M$.

3.2.6. Adaptive averaging

When the penalty interface condition is applied to the linear equations, the differences of the state vectors or their derivatives at the interfaces are spectrally so small that no additional conditions are needed. When, however, it is applied to highly non-linear problems such as the current reactive system, the differences at the interface can grow in time. Especially the growth of the differences in the first derivatives can induce the numerical instability. This implies that the constraint on the penalty parameters is, in fact, derived from the stability conditions of the linearized equations and it does not ensure the accuracy when it is applied to the non-linear problem due to the fact that the time interval cannot be arbitrarily small. To ensure the stability of the scheme at some particular collocation points where the solution become singular and unstable, we use the averaging method adaptively at selective grid points. In particular, we switched from the penalty method to the averaging when the following criteria was satisfied:

$$\max\left(\frac{|\rho - \rho_-|}{|\rho + \rho_-|}, \frac{|T - T_-|}{|T + T_-|}\right) \geqslant C_{\text{ave}}, \tag{54}$$

or

$$\frac{|P - P_-|}{|P + P_-|} \geqslant C_{\text{ave}}, \tag{55}$$

where C_{ave} is a non-negative constant. Note that $C_{\text{ave}} = 0$ leads to the averaging method, whereas a large C_{ave} results in the penalty method. For the value of C_{ave} used in this paper, we found out that there were very few points in which one needs to switch from the penalty to the averaging procedure. Moreover, this happened only at very few time steps.

4. The cavity system and numerical configurations

In this section we describe the set up of the simulations of the recessed cavity flame-holders by the spectral multidomain technique presented above. The main goal of this experiment is to investigate *how the geometry of the aft wall affects the flame stability*.

4.1. Physical setup

In the SCRAMJet community, a cavity with the length-to-depth ratio $L/D < 7 \sim 10$ is usually categorized as an 'open' cavity since the upper shear layer re-attaches at the back face [2]. In this work, we choose the L/D of the baseline cavity to be 4 and thus the open cavity system is considered. The coordinates of the cavity are $(7, -1 \text{ cm})$ for the upper left and $(11, -2 \text{ cm})$ for the right bottom corners of cavity. With the length of the neck of the cavity fixed to be 4 cm, we consider three different angles of the right corner of the floor of the

cavity (60°, 45° and 30°), we then compare each one with the case of the rectangular aft wall. The fluid conditions are given as followings; the free stream Mach number $M = 1.91$, total pressure $P = 2.82$ (atm), total temperature $T = 830.6$ (K) and normalized Reynolds number $R_e = 3.9 \times 10^7$ (m^{-1}). Note that the Reynolds number is here normalized and has a unit of [length]$^{-1}$, also the Reynolds number based on the cavity dimensions is O(10^5). The boundary layer thickness scale is $\delta = 5 \times 10^{-4}$ (m), and finally, the wall temperature is $T_w = 460.7835$ (K). The initial configuration for the baseline cavity system is shown in Fig. 2.

4.2. Numerical setup

We have conducted two different experiments for each of the following cases: (1) *non-reacting cold flow*, and (2) *reacting flow*. We use nine and 17 sub-domains for both cases. For the outflow conditions at the exit of the system and at the upper boundary, we mainly use a semi-infinite mapping in order to reduce the possible reflections at the boundaries. The characteristic boundary conditions are also applied and will be discussed in the next section and compared to the mapping. For the case of the reactive flows, the cavity was initially filled with hydrogen fuel with fuel-to-total gas ratio of 0.5. The order of the polynomial of approximation in y-direction in the domain beside the wall is taken large enough to resolve the boundary layer well. Finally the adaptive filtering is turned on if the mass fraction of hydrogen and oxygen exceed the range of $-0.09 \leqslant f_{H_2} \leqslant 1.09, -0.02 \leqslant f_{O_2} \leqslant 0.25$ and the temperature exceeds the range of 300 (K) $\leqslant T \leqslant 3500$ (K). As the shear layer and the complex features of the flows develop, the adaptivity criteria for applying the local smoothing is satisfied at some points. In the calculations, we use the third- and second-order local filtering for the non-reactive and reactive flows respectively. It turns out that the local smoothing was applied in very few points at the upper corner of the cavity wall.

For the adaptive averaging, we use the criteria constant C_{ave} such that the difference of the state vectors (or pressure) between the two adjacent domains is less than 10%. In Fig. 3 the penalty Navier–Stokes equations were considered for the non-reactive cold flows. As evident from the contours of the density, the approximations were well matched at the interfaces. Here the outer boundary was approximated by using the characteristic conditions of the inviscid fluxes. The adaptive averaging, with the given adaptivity conditions above, took place at only a few points. The characteristic boundary conditions using the inviscid fluxes yield good results for both the problems of the density peak propagation and the non-reactive cold flows. As in Fig. 1, we observe that there exist penalty parameters satisfying the stability conditions that may induce reflecting modes at the interfaces [16].
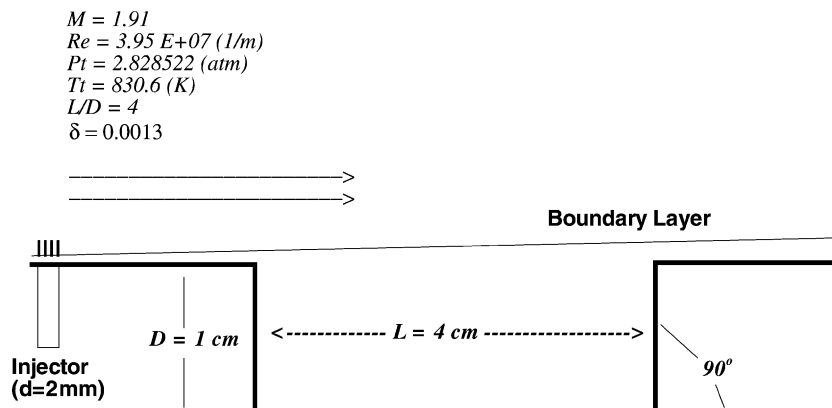

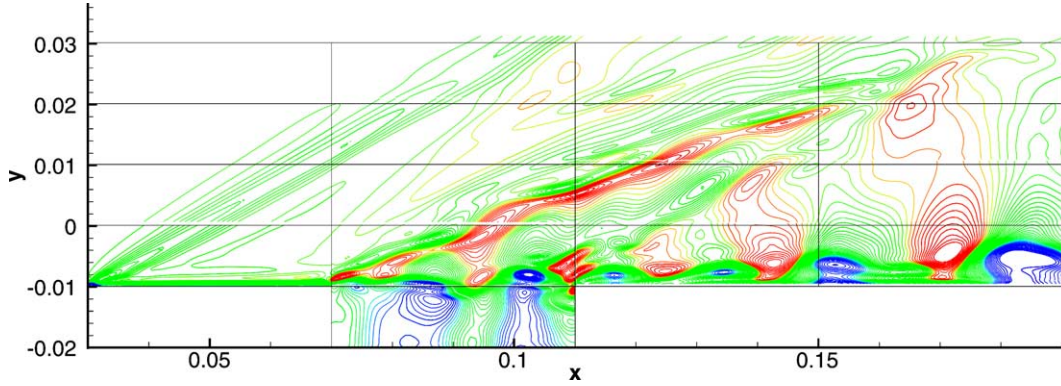Fig. 2. The initial configuration for the baseline cavity system.

Fig. 3. The non-reactive cold flows with the penalty Navier–Stokes equations: the density contours are given in this figure at $t = 0.25$ ms. Seventeen domains are used and the boundaries of each domain are shown.

4.3. Temporal and spatial approximation

We use the third-order TVD Runge–Kutta scheme [26] for the time integration. For the CFL condition we use the following restriction of the time interval Δt such that:

$$\Delta t \leqslant CFL \min(\Delta t_E, \Delta t_D, \Delta t_C, \Delta t_P),$$

where CFL is a positive constant and the subscripts E, D, C, and P denote the conditions by the convection, diffusion, chemical reaction and penalty parts of the governing equation of Eq. (31), respectively. And the time interval Δt is $\mathrm{O}(1/N^4)$. In the present work, we use the condition that $N = M$ and $\Delta^I = \Delta^{II}$ in order to make the method conservative both for the penalty and averaging interface treatment and reduce the possible reflecting modes induced at the interfaces as described in the previous section. For the spatial approximation, we first determine the mesh size in y-direction in order to resolve the boundary layer properly. The channel size l_c over the cavity and the boundary layer thickness scale δ are given by

$$l_c = 4 \times 10^{-2}, \quad \delta = 5 \times 10^{-4}.$$

By splitting the channel domain into n sub-domains, we determine the mesh size N in y-direction such that the boundary layer is well resolved as

$$\delta_N \equiv \frac{l_c/n}{N^2} \leqslant \delta.$$

In this work we use $n = 4$ and $N = 49$, and thus we obtain $\delta/\delta_N = 120.05$. Each domain is collocated by either 49 or 65 number of grid points in x- or y-direction. Thus the time interval Δt is about $\mathrm{O}(-8)$.

5. Results and discussion

5.1. Local adaptive filtering and adaptive averaging

In Section 3.1 we localize the filtering order γ in Eq. (18). Practically we define the local adaptive filtering with constant γ such as [27]

$$\sigma(\omega) = \exp(-\alpha|\omega|^{\gamma/c}), \tag{56}$$

where c is a positive controlling function such that $c \geqslant 1$ and $\alpha = -\ln \epsilon$ with the machine zero ϵ. By definition if $c = 1$ for all x, no local filtering is done but only the global filtering is carried out over the entire domain. At a certain grid point $x = x_i$, the controlling function is defined as

$$c = \begin{cases} 1 & \text{if } q^l(x_i, t) \leqslant q \leqslant q^u(x_i, t), \\ > 1 & \text{otherwise.} \end{cases} \tag{57}$$

Here q can be the mass fraction of each species f_i and/or temperature T and q^l and q^u denote the lower and upper tolerance limits of q. When the adaptivity condition represented by the above is satisfied at x_i, heavier filter than the global filter of order γ is applied at $x = x_i$. A local heavy smoothing is done *locally* where the sharp gradients inducing the numerical instability exist.

5.1.1. Global filtering

The method of determining γ has to be rather state-of-the-art if the solution is highly nonlinear and thus the exact solution is in general not known. For the current study we determine γ based on the *pressure-fluctuation-capturing constraint* by tracing the time-dependent pressure fluctuations inside the cavity. Experiments have shown that the highly oscillating non-transient pressure fluctuations in time are obtained with the flow conditions such as the ones used in this work [2,25,29]. Thus one needs to use γ that enables the method to capture these pressure fluctuations. If γ is taken to be too small, the method becomes too dissipative and, consequently, the pressure fluctuations decay with time, eventually yielding only the steady state solution inside the cavity. We determine γ empirically such that

$$\gamma > \gamma_0,$$

where γ_0 is the threshold smoothing order with the given N, ensuring that the method captures the highly oscillating non-transient pressure fluctuations inside the cavity. If $\gamma \leqslant \gamma_0$, the method is too dissipative and the method remains stable with no need of the local smoothing explained in the following. Thus the above criteria is the necessary condition for the method to be able to capture the pressure fluctuations. By the numerical experiments we find that the threshold order γ_0 exists in the following intervals:

$$4 < \gamma_0 < 6,$$

for the given $N \sim 49, 65$. If $\gamma \leqslant 4$, the method turns too dissipative whereas, if $\gamma \geqslant 6$, we clearly obtain the highly oscillating non-transient pressure fluctuations similar to the ones that we get through the laboratory experiments. Fig. 4 shows the pressure history when the heavy global filter is applied (in this case, the fourth-order filter was used). Unlike the case illustrated in Fig. 6, where the sixth-order global filter is used, the pressure fluctuations eventually decay out and a large recirculation zone is formed inside the cavity
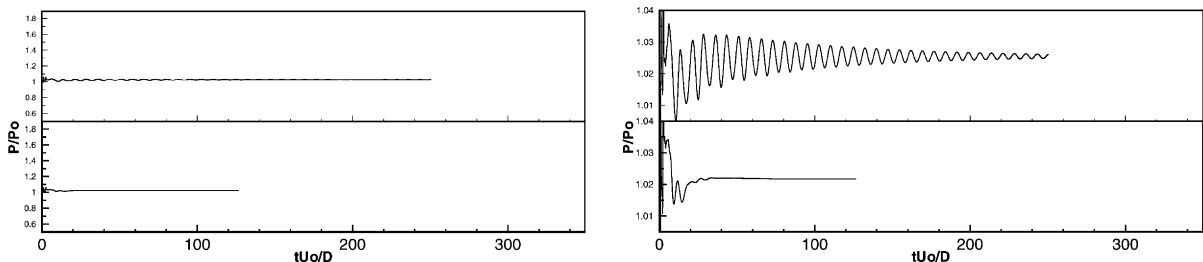

Fig. 4. Pressure history of the non-reactive flows with the use of the fourth-order filter: the left panel represents the pressure history at the center of cavity and the right panel shows the left panel in a smaller scale. Each panel shows the case of 90° and 30° cavity walls from top to bottom. Note that the scale of the right panel is different from the left.

without any severe pressure fluctuations. Note that the scale in the left panel shown is the same as in Fig. 6 while the right panel is shown in a smaller scale for a closer look. This figure shows that the large recirculation zone(s) formed inside the cavity obtained by the lower order numerical scheme is induced not physically but rather artificially due to the heavy numerical dissipations. This is clearly shown in Fig. 5. In this figure, a large recirculation zone is observed – this zone is formed earlier than these streamlines are captured – when the fourth-order filter is used (left figure) and an almost steady state is already reached as the pressure history indicates in Fig. 4. We find from the numerical results that the large recirculation is very stable once it forms. This large recirculation and the steady state solutions are not observed in the case of $\gamma = 6$ (right). For the case of $\gamma = 6$, not the large single recirculation zone but multiple smaller scale vortex circulations are formed and they are interacting with each other, never reaching the steady state with time. This result shows that high order filter should be used for these sensitive problems in order to minimize the effect of the numerical dissipation.

Here we note that if $\gamma > 6$, the pressure history profiles remain similar to that of $\gamma = 6$. For this reason, in the present study the sixth-order global smoothing ($\gamma = 6$) is used.

5.1.2. Local adaptive filtering

We observe the method is unstable with $\gamma > 6$ when $c = 1$ for all the collocation points. Thus c is adaptively determined by Eq. (57). In this work we choose the local controlling function c at the desired points such that $\gamma = 2$ or $\gamma = 3$ to reduce the magnitude of the oscillations sufficiently enough at those points. Although a heavy smoothing is applied, the desired flow structures and the pressure oscillations are expected not to be disturbed since it is applied only at a small number of points. Table 1 shows the frequency of the local filtering every 10 time integration steps starting from $t = 0.240039 \times 10^{-2}$ that is the time about the middle of the Fig. 6.

For this table, we use the data from the simulation of the non-reactive rectangular cavity flows with nine sub-domains. The corner of the aft wall is surrounded by the sixth, seventh and ninth domains. The second column of Table 1 shows for which sub-domain the local filter is applied and, in the parenthesis, the table shows how many times it is applied. The third column shows the ratio of the total number of the local filtering occurrence N_f to the total collocation points N_t of the given domain(s). The cavity domain (domain 9) has 65×65 collocation points, the domains 2 and 7 have 65×49 points and the others 49×49. Thus the total collocation points of the entire domain is 25,001. As shown in the table, the local filtering occurs only at a few points and every local smoothing occurs in the domains 6, 7 or 9 where the corner of the aft wall exists.

5.1.3. Adaptive averaging

For the adaptive criteria in Eqs. (54) and (55), we use $C_{ave} = 10$. As noted in Section 3 if $C_{ave} = 0$ the method is equivalent to the averaging scheme while if $C_{ave} \to \infty$ it is equivalent to pure penalty method without averaging. In Table 2 the frequency of the adaptive averaging every 10 time steps of the simulation of non-reactive cavity flow at $t = 5.044$ μs is provided. For this example we use $C_{ave} = 1$ and $\tau_1 = -1/2\omega_N$
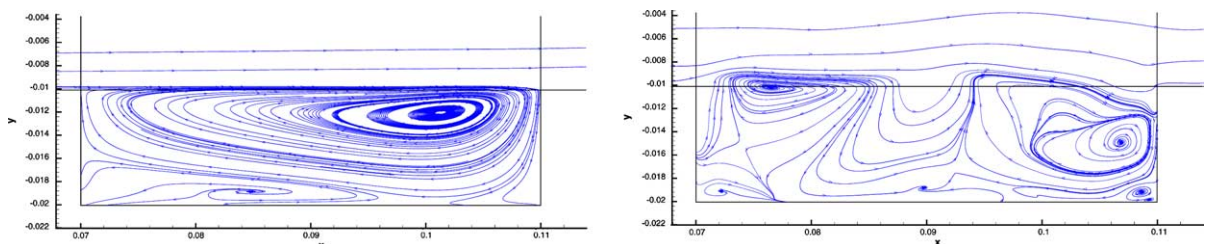

Fig. 5. Streamlines: the left figure shows the streamlines at $t = 1.685$ ms for the global filtering order $\gamma = 4$ and the right at $t = 2.38$ ms for $\gamma = 6$.
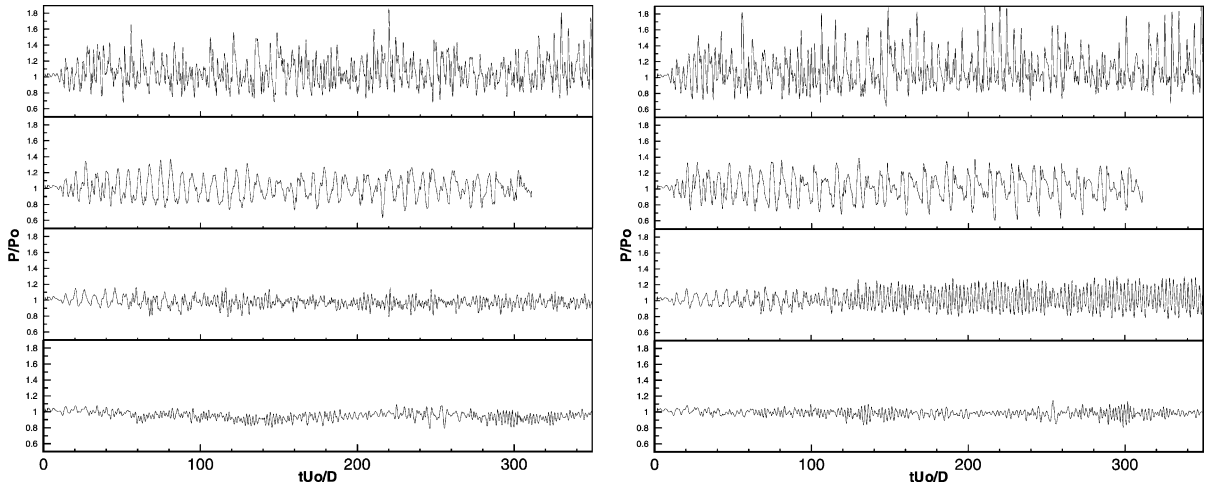
Fig. 6. Pressure history for non-reactive flows: the left panel represents the pressure history at the center of the cavity and the right panel at the middle of the floor of the cavity. Each panel shows the case of 90°, 60°, 45° and 30° cavity walls from top to bottom.

Table 1
Frequency of the local adaptive filtering for the non-reactive rectangular cavity flows

Step interval	Domain (frequency)	N_f/N_t
62,310–62,320	6(3)	3/2401
62,320–62,330	N/A	0
62,330–62,340	N/A	0
62,340–62,350	N/A	0
62,350–62,360	N/A	0
62,360–62,370	N/A	0
62,370–62,380	9(1)	1/4225
62,380–62,390	NA	0
62,390–62,400	9(2)	2/4225
62,400–62,410	N/A	0
62,410–62,420	9(1)	1/4225
62,420–62,430	9(1)	1/4225
62,430–62,440	9(2)	2/4225
62,440–62,450	9(3)	3/4225
62,450–62,460	7(1), 9(3)	4/7410
62,460–62,470	7(1)	1/3185
62,470–62,480	7(3), 9(4)	7/7410
62,480–62,490	N/A	0
62,490–62,500	7(6)	6/3185
62,500–62,510	7(1)	1/3185
62,510–62,520	7(2)	2/3185
62,520–62,530	7(2)	2/3185
62,530–62,540	7(2)	2/3185
62,540–62,550	7(2), 9(1)	3/7410
62,550–62,560	7(1), 9(1)	2/7410
62,560–62,570	7(2), 9(1)	3/7410
62,570–62,580	9(2)	2/4225
62,580–62,590	7(2), 9(2)	4/7410
62,590–62,600	9(2)	2/4225

Total collocation points = 25,001.

Table 2
Frequency of the adaptive averaging for the non-reactive rectangular cavity flows during 10 time steps

Domain	Frequency	N_b
1	2	228
2	8	196
3	8	196
4	6	196
5	10	196
6	12	196
7	14	196
8	4	228
9	2	228
10	14	196
11	16	196
12	12	196
13	6	196
14	8	196
15	5	196
16	1	228
17	0	196

and $\tau_2 = N/2\omega_N$ with 17 sub-domains. The second column shows how many times the adaptive averaging is applied during the given interval and the third column gives the number of collocation points at the interfaces of the specific sub-domain. Since $C_{ave} = 1 < 10$ for this case, we note that more frequent averaging should be used than the case of $C_{ave} = 10$.

5.2. Pressure history

Fig. 6 shows the pressure history of the non-reactive cold flows for the various angles of the aft wall at two different locations inside the cavity, i.e., at the center, $(x, y) = (8.5, 1.5 \text{ cm})$, and at the middle of the floor $(x, y) = (8.5, -1.9 \text{ cm})$.

These figures show that the pressure fluctuations in cavities with lower angle of the aft are weaker than in cavities with higher angles. It is also shown that the attenuation of the pressure fluctuations are obtained both at the center and the middle of the floor of the cavity. It is interesting to observe that the patterns of the pressure fluctuations for a given angle at different locations are different depending on the angle. In the case of the 30° aft wall, the pressure fluctuations are almost the same at the two locations considered whereas the case of 45° shows a difference in the patterns of the pressure fluctuations between the two locations. The pressure fluctuations at the bottom grows greater than that at the center after some time.

Fig. 4 shows the pressure history when the heavy global filter is applied (in this case, the fourth-order filter was used). Unlike the previous case illustrated in Fig. 6, where the sixth-order global filter is used, the pressure fluctuations eventually decay out and a large recirculation zone is formed inside the cavity without any severe pressure fluctuations. Note that the scale in the left panel shown is the same as in Fig. 6 while the right panel is shown in a smaller scale for a closer look. This figure shows that the large recirculation zone(s) formed inside the cavity obtained by the lower order numerical scheme is induced not physically but rather artificially due to the heavy numerical dissipations. This is clearly shown in Fig. 5. In this figure a large recirculation zone is observed – this zone is formed earlier than this streamlines are captured – when the fourth-order filter is used (left figure) and an almost steady state is already reached as the pressure history indicates in Fig. 4. We find from
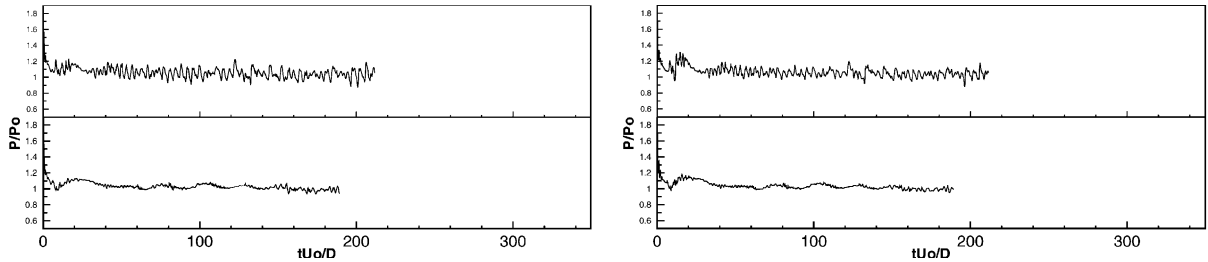
Fig. 7. Pressure history for reactive flows: the left panel represents the pressure history at the center of cavity and the right panel at the middle of the floor of cavity. Each panel shows the case of 90° and 30° cavity walls from top-to-bottom.
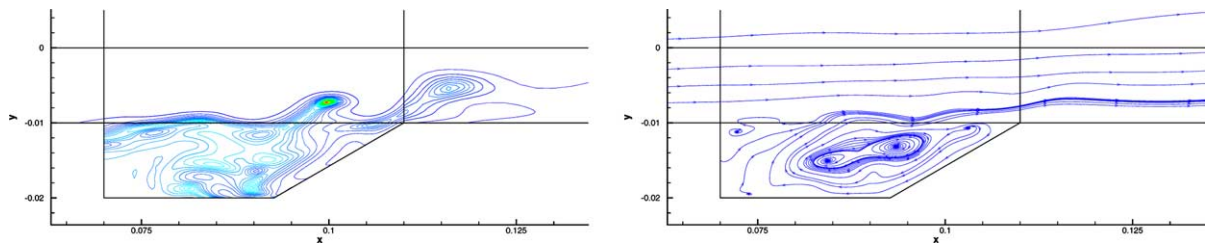

Fig. 8. The water contour of the reactive flows: the water density contour is given in the left figure and its streamlines in the right figure at $t = 0.135$ ms.

the numerical results that the large recirculation is very stable once it forms. This large recirculation and the steady state solutions are not observed in the case of $\gamma = 6$ (right). For the case of $\gamma = 6$ instead of the large single recirculation zone, smaller scale vortex circulations are formed and they are interacting with each other, never reaching the steady state with time. This result shows that for these sensitive problems, high order accuracy should be used in order to minimize the effect of the numerical dissipation.

Figs. 7 and 8 show the case of the reactive flows for the 90° and 30° aft walls. Similar features of the pressure fluctuations are shown as in the non-reactive flows. However the pressure fluctuations are much more attenuated for both the 90° and 30° walls than in the non-reactive cold flows (Fig. 7). In the reactive cases hydrogen fuel, which was initially supplied inside the cavity was consumed. As time elapses, the fuel is consumed out with the production of the water for these cases (Fig. 8).

These results demonstrate that simulations of cold flows do not necessarily shed light on the behavior of reactive flows.

5.3. Flow fields

5.3.1. Non-reactive cold flow

Fig. 9 shows the density contours and streamlines for the 90°, 60°, 45° and 30° walls at the instant time $t = 2.4$ ms. As shown in the figure, the shear layer is becoming weaker as the degree of angle of the aft wall and the flow fields are becoming more regularized for the case of the lower angle. And note that the density compression at the corner of the aft wall is also becoming weaker for the more slanted wall cases.
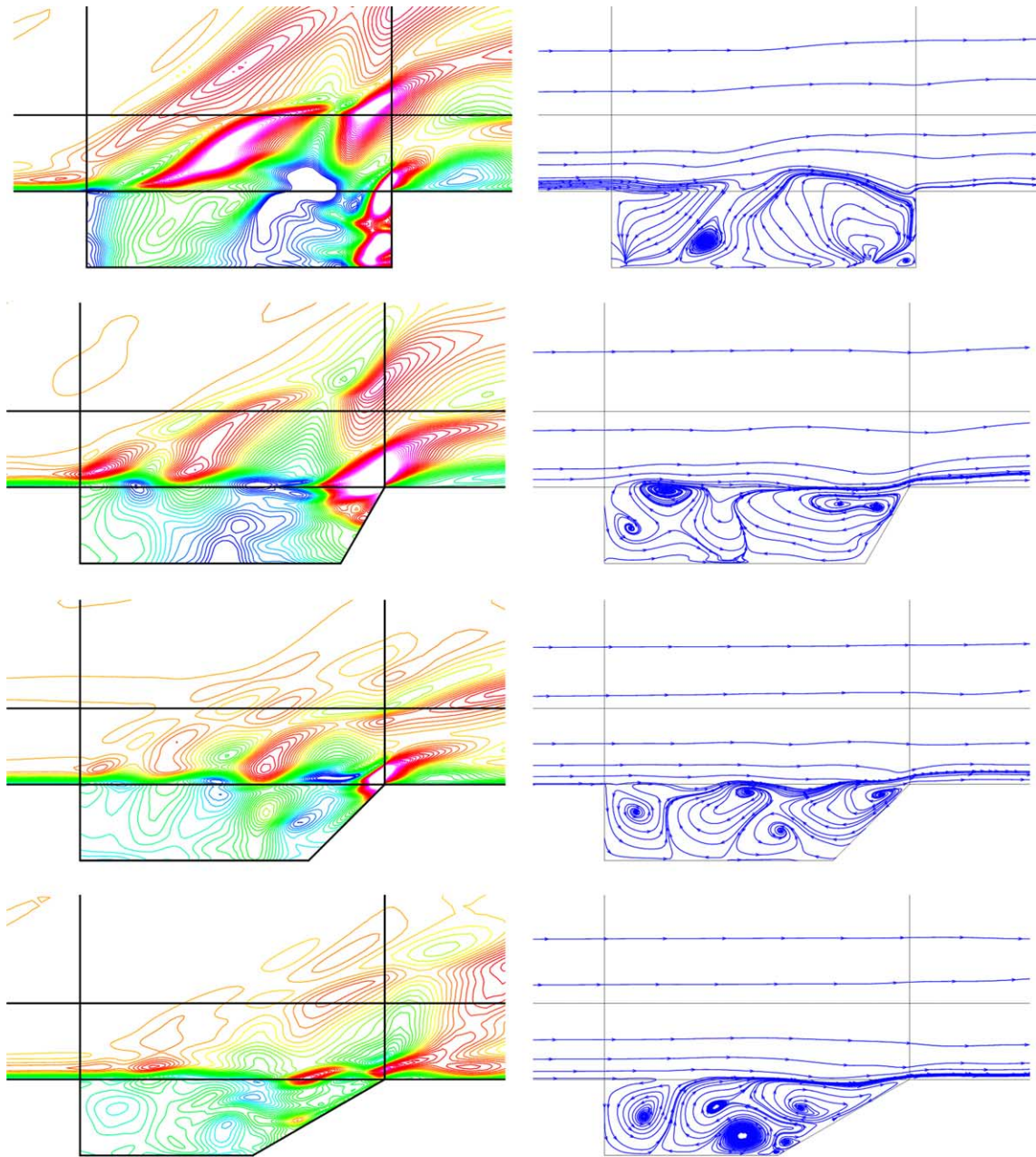
Fig. 9. The density contour and the streamline of the non-reactive flows: the left column shows the density contour for 90°, 60°, 45° and 30° walls from top to bottom and the right column shows the corresponding streamlines at $t = 2.43$ ms. The maximum contour level is 1.8 and the minimum 0.5 with the level step size 50.

Fig. 11 shows the streamlines corresponding to the each case of Fig. 10. Note that compared to the non-reactive cases, the shear layers are less developed for the reactive cases. As the figures of the pressure fluctuation history and Fig. 11 indicate, the shear layers are weak for both the 90° and the 30° walls in the reactive cases.
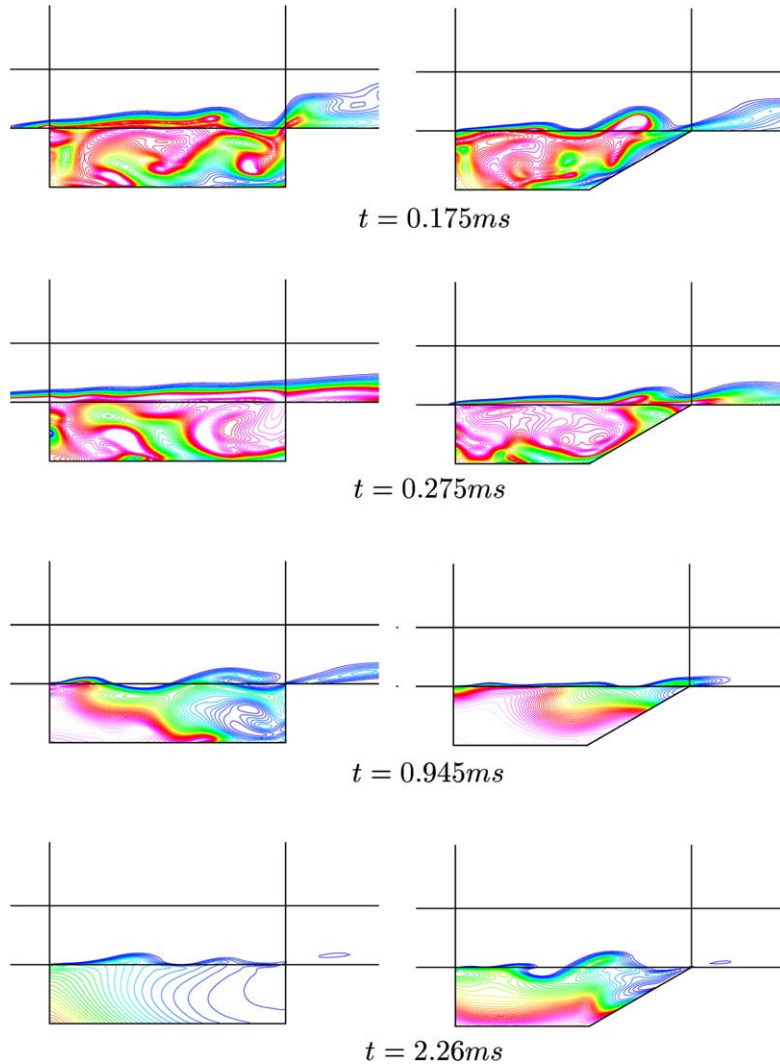
Fig. 10. The water contour of the reactive flows: the water density contours are given in the left figures for 90° wall and 30° wall in the right figures. From top to bottom the instant times t are 0.175, 0.275, 0.945 and 2.26 ms. The maximum and minimum contour levels are 0.01 and 0.23, respectively, with the number of levels 50.

5.3.2. Reactive flow

Fig. 10 shows the water contour inside the cavity for the different angles at different time. Here we define the region where the flames are generated to be same as the region where the water is produced. As the hydrogen fuel is consumed, the water is produced and starts to be expelled from the cavity to the main channel. The flame-holding efficiency is enhanced if the chemical radicals (water in this case) are stably circulating and long lasting before they are expelled from the cavity. Fig. 10 shows that the lower angled aft wall (30° in this case) maintains more water than the 90° wall at a given time. The figure also shows that the lower angled aft wall holds the flame (water in this case) longer than the 90° wall – in the last figure in
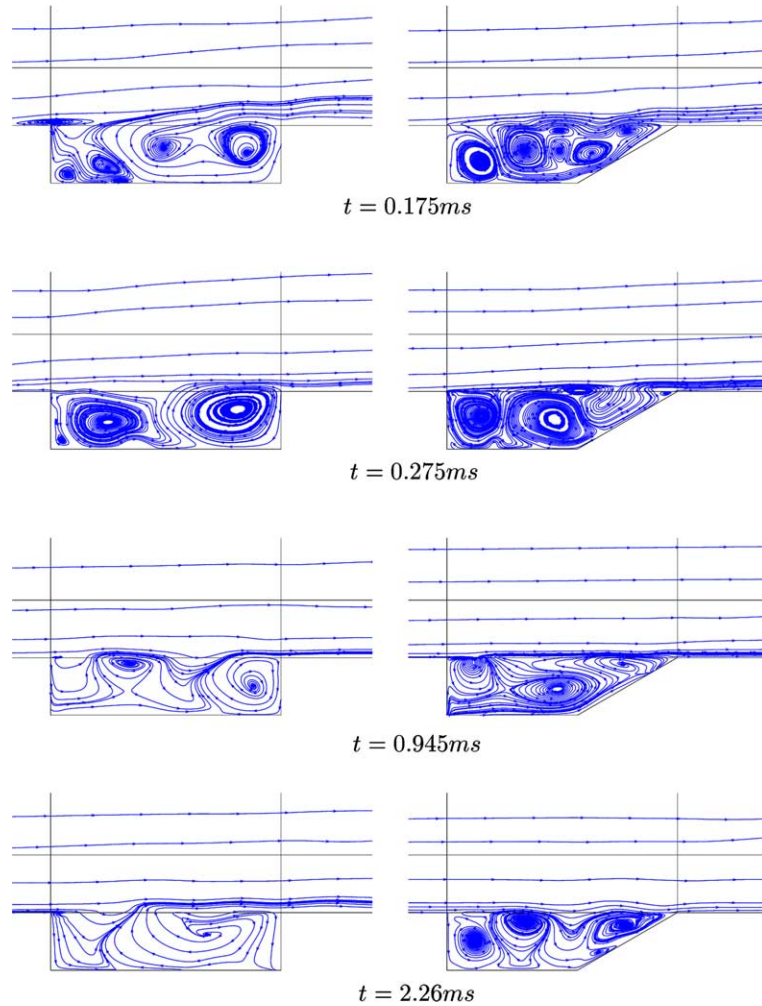
Fig. 11. The streamlines for the reactive flows: the streamlines for 90° wall are shown in the left figures and the 30° wall in the right. From top to bottom the times t are 0.175, 0.275, 0.945 and 2.51 ms.

Fig. 10 at $t = 2.26$ ms, the most water is expelled and only the small amount is left in the left corner while the 30° wall cavity holds the water still throughout the cavity. These results imply that the flame-holding efficiency can be increased by lowering the angle of the aft wall of the cavity.

Appendix A. The similarity transform matrices and the eigenvalues of the inviscid flux with chemical species

A.1. Air model without combustion

First consider the ideal gas composed of two chemically non-reactive species (for the ideal mono-atomic gas Λ the diagonal matrix and S, the diagonalizer, were given in [15]). Λ is given by

$$\Lambda = \mathrm{diag}(\vec{U} \cdot \vec{n} + c, \vec{U} \cdot \vec{n}, \vec{U} \cdot \vec{n}, \vec{U} \cdot \vec{n} - c, \vec{U} \cdot \vec{n}, \vec{U} \cdot \vec{n}),$$

where $\vec{U} = (u, v)$, $\vec{n} = (n_x, n_y)$ is an unit outward normal vector at the interface and c is a local sound speed.

For simplicity we assume that

$$\rho \int_0^T \bar{C}_p(s)\, \mathrm{d}s - P \sim \rho C_v T.$$

This form is used only in the analysis, as mentioned in Section 3.1, C_{p_i} is expressed as a fourth-order polynomial in the temperature T. The nonlinear expression of C_{p_i} makes it difficult to derive the Jacobian matrices of the fluxes. Our simplifications is a results of assuming small coefficients of the high order terms of the polynomial. In the actual simulations C_v is computed appropriately using the empirical law and assumed temperature independent at each linearization step. With this assumption S is given by

$$S = \begin{pmatrix}
1 & 1 & 0 & 1 & 0 & 0 \\
u + cn_x & u & -n_y & u - cn_x & 0 & -n_y \\
v + cn_y & v & n_x & v - cn_y & 0 & n_x \\
H + c\vec{U}\cdot\vec{n} & \frac{1}{2}\vec{U}\cdot\vec{U} & \vec{U}\cdot\vec{k} & H - c\vec{U}\cdot\vec{n} & \beta c^2 & \vec{U}\cdot\vec{k} + c \\
f_1 & a_{12} & 0 & f_1 & a_{12} & -c\frac{R_2}{R_h} \\
f_2 & a_{21} & 0 & f_2 & a_{21} & c\frac{R_1}{R_h}
\end{pmatrix},$$

where $H = (E + P)/\rho$, $R_i = R/(M_i C_v)$, $R_h = R_1 h_2^0 - R_2 h_1^0$, $R_v = \sum_{i=1}^2 f_i R_i$, $\beta = -1/(R_v + R_v^2)$, the tangential vector $\vec{k} = (-n_y, n_x)$ and

$$a_{ij} = R_v \frac{h_j^0}{(R_i h_j^0 - R_j h_i^0)}, \qquad a_{ji} = R_v \frac{h_i^0}{(R_j h_i^0 - R_i h_j^0)}.$$

Note that $R_v = \gamma - 1$ for the mono-atomic ideal gas with γ, the ratio between the heat capacities C_p and C_v.

A.2. Air model with combustion

Consider now the equations the Euler equations with four reactive species. In this case Λ and S are given by

$$\Lambda = \mathrm{diag}(\vec{U}\cdot\vec{n} + c, \vec{U}\cdot\vec{n}, \vec{U}\cdot\vec{n}, \vec{U}\cdot\vec{n} - c, \vec{U}\cdot\vec{n}, \vec{U}\cdot\vec{n}, \vec{U}\cdot\vec{n}, \vec{U}\cdot\vec{n})$$

and

$$S = \begin{pmatrix}
1 & 1 & 0 & 1 & 0 & 0 & 1 & 1 \\
u + cn_x & u & -n_y & u - cn_x & 0 & -n_y & u & u \\
v + cn_y & v & n_x & v - cn_y & 0 & n_x & v & v \\
H + c\vec{U}\cdot\vec{n} & \frac{1}{2}\vec{U}\cdot\vec{U} & \vec{U}\cdot\vec{k} & H - c\vec{U}\cdot\vec{n} & \beta c^2 & \vec{U}\cdot\vec{k} + c & \frac{1}{2}\vec{U}\cdot\vec{U} & \frac{1}{2}\vec{U}\cdot\vec{U} \\
f_1 & a_{12} & 0 & f_1 & a_{1234} & R_{1234} & a_{13} & a_{14} \\
f_2 & a_{21} & 0 & f_2 & a_{2134} & R_{2134} & 0 & 0 \\
f_3 & 0 & 0 & f_3 & a_{3124} & R_{3124} & a_{31} & 0 \\
f_4 & 0 & 0 & f_4 & a_{4123} & R_{4123} & 0 & a_{41}
\end{pmatrix},$$

where all the variables are same as in the two species case except that

$$a_{ijkl} = \epsilon_{ijkl}\left(h_j^0 - h_k^0 + h_l^0\right)R_v/R_h$$

and

$$R_{ijkl} = -\epsilon_{ijkl}(R_j - R_k + R_l)c/R_h,$$

with

$$R_h = \sum_{i=1}^4 \epsilon_{ijkl}R_i\left(h_j^0 - h_k^0 + h_l^0\right), \qquad i,j,k,l = 1,2,3,4, \quad j < k < l.$$

ϵ_{ijkl} is the permutation symbol and $R_v = \sum_{i=1}^4 f_i R_i$. Λ and S are based on the time dependent local spatial quantities at a given time. $f^\pm$ is calculated at the interface points at each time.

Appendix B. The symmetrizability of the coefficient matrices of the Navier–Stokes equations with chemical species

In [1] it had been proven that the coefficient matrices of the Navier–Stokes equations (expressed in the primitive form), of the ideal gas can be simultaneously symmetrized. In [12,15] the same result was demonstrated for the conservative form of the equations. Here we show that it is also true for the Navier–Stokes equations of the combustible gas with multiple chemical species in two dimension.

Rewrite the linearized Navier–Stokes equations (2) in conservative form without the chemical source term as

$$\frac{\partial q}{\partial t} + \mathbf{A}\frac{\partial q}{\partial x} + \mathbf{B}\frac{\partial q}{\partial y} = \mathbf{C}\frac{\partial^2 q}{\partial x^2} + \mathbf{D}\frac{\partial^2 q}{\partial x \partial y} + \mathbf{E}\frac{\partial^2 q}{\partial y^2},$$

where

$$\mathbf{A} = \frac{\partial F}{\partial q}, \quad \mathbf{B} = \frac{\partial G}{\partial x}, \quad \mathbf{C} = \frac{\partial F_v}{\partial q_x}, \quad \mathbf{D} = \frac{\partial}{\partial q_y} + \frac{\partial G_v}{\partial q_x} \quad \text{and} \quad \mathbf{E} = \frac{\partial G_v}{\partial q_y}.$$

It is sufficient to consider the chemically interacting two chemical species. The coefficient matrices are given by

$$\mathbf{A} = \begin{pmatrix} 0 & 1 & 0 & 0 & 0 & 0 \\ \chi - u^2 & (2 - R_v)u & -R_v v & R_v & \psi_1 & \psi_2 \\ -uv & v & u & 0 & 0 & 0 \\ u(\chi - H) & H - R_v u^2 & -R_v uv & (1 + R_v)u & u\psi_1 & u\psi_2 \\ -uf_1 & f_1 & 0 & 0 & u & 0 \\ -uf_2 & f_2 & 0 & 0 & 0 & u \end{pmatrix},$$

$$\mathbf{B} = \begin{pmatrix} 0 & 0 & 1 & 0 & 0 & 0 \\ -uv & v & u & 0 & 0 & 0 \\ \chi - v^2 & -R_v u & (2 - R_v)v & R_v & \psi_1 & \psi_2 \\ v(\chi - H) & -R_v uv & H - R_v v^2 & (1 + R_v)v & v\psi_1 & v\psi_2 \\ -vf_1 & 0 & f_1 & 0 & v & 0 \\ -vf_2 & 0 & f_2 & 0 & 0 & v \end{pmatrix},$$

$$\mathbf{C} = \begin{pmatrix} 0 & 0 & 0 & 0 & 0 & 0 \\ -u\sigma_1 & \sigma_1 & 0 & 0 & 0 & 0 \\ -v\sigma_2 & 0 & \sigma_2 & 0 & 0 & 0 \\ -\Sigma_{12} & u(\sigma_1 - \sigma_3) & v(\sigma_2 - \sigma_3) & \sigma_3 & \delta_1 & \delta_2 \\ 0 & 0 & 0 & 0 & 0 & 0 \\ 0 & 0 & 0 & 0 & 0 & 0 \end{pmatrix},$$

$$\mathbf{D} = (\sigma_1 - \sigma_2) \begin{pmatrix} 0 & 0 & 0 & 0 & 0 & 0 \\ -v & 0 & 1 & 0 & 0 & 0 \\ -u & 1 & 0 & 0 & 0 & 0 \\ -2uv & v & u & 0 & 0 & 0 \\ 0 & 0 & 0 & 0 & 0 & 0 \\ 0 & 0 & 0 & 0 & 0 & 0 \end{pmatrix},$$

$$\mathbf{E} = \begin{pmatrix} 0 & 0 & 0 & 0 & 0 & 0 \\ -u\sigma_2 & \sigma_2 & 0 & 0 & 0 & 0 \\ -v\sigma_1 & 0 & \sigma_1 & 0 & 0 & 0 \\ -\Sigma_{21} & u(\sigma_2 - \sigma_3) & v(\sigma_1 - \sigma_3) & \sigma_3 & \delta_1 & \delta_2 \\ 0 & 0 & 0 & 0 & 0 & 0 \\ 0 & 0 & 0 & 0 & 0 & 0 \end{pmatrix},$$

where

$$U_2 = \frac{1}{2}\vec{U} \cdot \vec{U}, \quad H = \frac{E+P}{\rho}, \quad \sigma_1 = \frac{2\mu + \lambda}{\rho}, \quad \sigma_2 = \frac{\mu}{\rho}, \quad \sigma_3 = \mu\frac{\bar{C}_p}{\rho P_r C_v},$$

$$\zeta = \frac{P}{\rho R_v}, \quad \chi = R_v(U_2 - \zeta), \quad \psi_i = \zeta R_i - R_v h_i^0, \quad \delta_i = -h_i f_i \frac{\mu}{\rho S_c}, \quad \tilde{\delta}_i = -\frac{\delta_i}{\sigma_3},$$

$$\xi = \frac{E}{\rho} + \sum_{i=1}^{2}(h_i - \tilde{\delta}_i)f_i, \quad \theta = \xi - 2U_2 \quad \text{and} \quad \Sigma_{jk} = \sigma_j u^2 + \sigma_k v^2 + \sigma_3 \theta.$$

To find the symmetrizer for $\mathbf{A}$, $\mathbf{B}$, $\mathbf{C}$, $\mathbf{D}$ and $\mathbf{E}$, we first consider the similarity transform matrix $\mathbf{S}_P$ of $\mathbf{C}$ such that

$$\mathbf{S}_P^{-1}\mathbf{C}\mathbf{S}_P = \Lambda_C,$$

where Λ_C is a diagonal matrix composed of the eigenvalues of $\mathbf{C}$. The subscript P denotes that this matrix is adopted from the parabolic portion of the equations [1]. The diagonal matrix Λ_C of $\mathbf{C}$ is given by

$$\Lambda_C = \begin{pmatrix} 0 & 0 & 0 & 0 & 0 & 0 \\ 0 & \sigma_1 & 0 & 0 & 0 & 0 \\ 0 & 0 & \sigma_2 & 0 & 0 & 0 \\ 0 & 0 & 0 & \sigma_3 & 0 & 0 \\ 0 & 0 & 0 & 0 & 0 & 0 \\ 0 & 0 & 0 & 0 & 0 & 0 \end{pmatrix}.$$

The diagonalizer $\mathbf{S}_P$ is composed of the eigenvectors of $\mathbf{C}$, $\mathbf{S}_P$ and its inverse $\mathbf{S}_P^{-1}$ are given by

$$\mathbf{S}_P = \begin{pmatrix} 1 & 0 & 0 & 0 & 0 & 0 \\ u & 1 & 0 & 0 & 0 & 0 \\ v & 0 & 1 & 0 & 0 & 0 \\ \zeta & u & v & 1 & \tilde{\delta}_1 & \tilde{\delta}_2 \\ 0 & 0 & 0 & 0 & 1 & 0 \\ 0 & 0 & 0 & 0 & 0 & 1 \end{pmatrix}, \quad \mathbf{S}_P^{-1} = \begin{pmatrix} 1 & 0 & 0 & 0 & 0 & 0 \\ -u & 1 & 0 & 0 & 0 & 0 \\ -v & 0 & 1 & 0 & 0 & 0 \\ -\theta & -u & -v & 1 & -\tilde{\delta}_1 & -\tilde{\delta}_2 \\ 0 & 0 & 0 & 0 & 1 & 0 \\ 0 & 0 & 0 & 0 & 0 & 1 \end{pmatrix}.$$

The similarity transform induced by $\mathbf{S}_P$, transforms the coefficient matrices $\mathbf{A}$, $\mathbf{B}$, $\mathbf{C}$, $\mathbf{D}$ and $\mathbf{E}$ to

$$\mathbf{S}_P^{-1}\mathbf{A}\mathbf{S}_P = \begin{pmatrix} u & 1 & 0 & 0 & 0 & 0 \\ \alpha & u & 0 & R_v & \eta_1 & \eta_2 \\ 0 & 0 & u & 0 & 0 & 0 \\ 0 & R_v\zeta & 0 & u & 0 & 0 \\ 0 & f_1 & 0 & 0 & u & 0 \\ 0 & f_2 & 0 & 0 & 0 & u \end{pmatrix},$$

$$\mathbf{S}_P^{-1}\mathbf{B}\mathbf{S}_P = \begin{pmatrix} v & 0 & 1 & 0 & 0 & 0 \\ 0 & v & 0 & 0 & 0 & 0 \\ \alpha & 0 & v & R_v & \eta_1 & \eta_2 \\ 0 & 0 & R_v\zeta & v & 0 & 0 \\ 0 & 0 & f_1 & 0 & v & 0 \\ 0 & 0 & f_2 & 0 & 0 & v \end{pmatrix},$$

$$\mathbf{S}_P^{-1}\mathbf{D}\mathbf{S}_P = \begin{pmatrix} 0 & 0 & 0 & 0 & 0 & 0 \\ 0 & 0 & 1 & 0 & 0 & 0 \\ 0 & 1 & 0 & 0 & 0 & 0 \\ 0 & 0 & 0 & 0 & 0 & 0 \\ 0 & 0 & 0 & 0 & 0 & 0 \\ 0 & 0 & 0 & 0 & 0 & 0 \end{pmatrix},$$

$$\mathbf{S}_P^{-1}\mathbf{E}\mathbf{S}_P = \begin{pmatrix} 0 & 0 & 0 & 0 & 0 & 0 \\ 0 & \sigma_2 & 0 & 0 & 0 & 0 \\ 0 & 0 & \sigma_1 & 0 & 0 & 0 \\ 0 & 0 & 0 & \sigma_3 & 0 & 0 \\ 0 & 0 & 0 & 0 & 0 & 0 \\ 0 & 0 & 0 & 0 & 0 & 0 \end{pmatrix},$$

where $\alpha = R_v\theta - \chi$ and $\eta_i = R_v(\tilde{\delta}_i + h_1 f_1) + \psi_i$.

Introducing a symmetrizing diagonal matrix, $\mathbf{Q}^{\mathrm{T}}\mathbf{Q}$ such as

$$\mathbf{Q}^{\mathrm{T}}\mathbf{Q} = \begin{pmatrix} \alpha & 0 & 0 & 0 & 0 & 0 \\ 0 & 1 & 0 & 0 & 0 & 0 \\ 0 & 0 & 1 & 0 & 0 & 0 \\ 0 & 0 & 0 & \frac{1}{\zeta} & 0 & 0 \\ 0 & 0 & 0 & 0 & \frac{\eta_1}{f_1} & 0 \\ 0 & 0 & 0 & 0 & 0 & \frac{\eta_2}{f_2} \end{pmatrix}$$

we have symmetrized all the coefficient matrices, i.e.,

$$\mathbf{Q}^T\mathbf{Q}\mathbf{S}_P^{-1}\mathbf{A}\mathbf{S}_P = \left(\mathbf{Q}^T\mathbf{Q}\mathbf{S}_P^{-1}\mathbf{A}\mathbf{S}_P\right)^T,$$
$$\mathbf{Q}^T\mathbf{Q}\mathbf{S}_P^{-1}\mathbf{B}\mathbf{S}_P = \left(\mathbf{Q}^T\mathbf{Q}\mathbf{S}_P^{-1}\mathbf{B}\mathbf{S}_P\right)^T,$$
$$\mathbf{Q}^T\mathbf{Q}\mathbf{S}_P^{-1}\mathbf{C}\mathbf{S}_P = \left(\mathbf{Q}^T\mathbf{Q}\mathbf{S}_P^{-1}\mathbf{C}\mathbf{S}_P\right)^T,$$
$$\mathbf{Q}^T\mathbf{Q}\mathbf{S}_P^{-1}\mathbf{D}\mathbf{S}_P = \left(\mathbf{Q}^T\mathbf{Q}\mathbf{S}_P^{-1}\mathbf{D}\mathbf{S}_P\right)^T,$$
$$\mathbf{Q}^T\mathbf{Q}\mathbf{S}_P^{-1}\mathbf{E}\mathbf{S}_P = \mathbf{S}_P^{-1}\mathbf{E}\mathbf{S}_P.$$

Appendix C. Constants for chemical models

Here we provide constants used in the chemical model for the current numerical experiment. Table 3 gives the constants used to get the approximation of the specific heat C_{p_i} of ith species in the fourth-order polynomial of T, i.e.,

$$C_{p_i} = (c_1 + T(c_2 + T(c_3 + T(c_4 + c_5 T))))R/M_i,$$

where R is a gas constant, and M_i is a molecular weight of ith species [20].

Table 4 gives the molecular weight and specific enthalpy for each chemical species and Table 5 gives the reference dynamic viscosity, temperature constants T and S in Wilke's law [28].

Table 3
Coefficients for the approximation of the specific heat C_{p_i}

	O_2	H_2	H_2O	N_2
c_1 (mol^{-1})	3.0809	3.4990	3.4990	3.1459
c_2 (mol^{-1})	0.16962E−2	−0.18651E−3	0.14878E−2	0.99154E−3
c_3 (mol^{-1})	−0.76334E−6	0.46064E−6	0.87544E−7	−0.22912E−6
c_4 (mol^{-1})	0.17140E−9	−0.13157E−9	−0.11499E−9	0.12181E−10
c_5 (mol^{-1})	−0.14116E−13	0.11679E−13	0.13495E−13	0.11024E−14

Table 4
Molecular weights and specific enthalpy

	O_2	H_2	H_2O	N_2
M (mol^{-1})	32.000	2.016	18.016	28.016
h^0 (J/kg)	−272918.21	−4280070.46	−13973684.55	−302736.23

Table 5
Constants for Wilke's law

	O_2	H_2	H_2O	N_2
μ_0 (kg/m/s)	0.1919E−4	0.08411E−4	0.1703E−4	0.1663E−4
T_0 (K)	273.111	273.111	416.667	273.111
S (K)	138.889	96.6667	861.111	106.667

References

[1] S. Abarbanel, D. Gottlieb, J. Comput. Phys. 41 (1981) 1.
[2] A. Ben-Yakar, R.K. Hanson, AIAA paper 98-3122, 1998.
[3] R.A. Baurle, M.R. Gruber, AIAA paper 98-0938, 1998.
[4] M.H. Carpenter, J. Nordström, D. Gottlieb, ICASE NASA-CR-206921, 1998.
[5] M.H. Carpenter, D. Gottlieb, C.-W. Shu, ICASE 2001-44, 2001.
[6] D.L. Davis, R.D.W. Bowersox, AIAA paper 97-3274, 1997.
[7] W.S. Don, D. Gottlieb, SIAM J. Numer. Anal. 35 (1998) 2370.
[8] W.S. Don, D. Gottlieb, AIAA 97-0538, 1997.
[9] W.S. Don, C.B. Quillen, J. Comput. Phys. 122 (1995) 244.
[10] D. Funaro, D. Gottlieb, Math. Comp. 51 (1988) 599.
[11] D. Funaro, D. Gottlieb, Math. Comp. 57 (1991) 585.
[12] A. Harten, J. Comput. Phys. 49 (1983) 151.
[13] J.S. Hesthaven, D. Gottlieb, SIAM J. Sci. Comput. 17 (1996) 579.
[14] J.S. Hesthaven, SIAM J. Sci. Comput. 18 (1997) 658.
[15] J.S. Hesthaven, SIAM J. Sci. Comput. 20 (1999) 62.
[16] J.H. Jung, Ph.D. Thesis, Brown University, 2002.
[17] H. Ma, SIAM J. Numer. Anal. 35 (1998) 893.
[18] Y. Maday, S. Ould Kaber, E. Tadmor, SIAM J. Numer. Anal. 30 (1993) 321.
[19] Y. Maday, E. Tadmor, SIAM J. Numer. Anal. 26 (1989) 854.
[20] B.J. McBride, S. Heimel, J.G. Ehlers, S. Gordon, NASA SP-3001, 1963.
[21] J. Nordström, M.H. Carpenter, J. Comput. Phys. 148 (1999) 621.
[22] J. Nordström, M.H. Carpenter, J. Comput. Phys. 173 (2001) 149.
[23] D.P. Rizzetta, AIAA J. 26 (7) (1988) 799.
[24] E. Tadmor, SIAM J. Numer. Math. 26 (1989) 30.
[25] M.B. Tracy, E.B. Plentovish, NASA Technical Memorandum 4436, 1993.
[26] C.W. Shu, S. Osher, J. Comput. Phys. 83 (1989) 32.
[27] H. Vandeven, J. Comput. Phys. 24 (1992) 37.
[28] C.R. Wilke, Chem. Phys. 18 (1950) 517.
[29] X. Zhang, J.A. Edwards, Aeronaut. J. 94 (940) (1990) 355.
[30] X. Zhang, A. Rona, J.A. Edwards, Aeronaut. J. (March) (1998) 129.